Aalborg Universitet

A sequential calibration approach based on the ensemble Kalman filter (C-EnKF) for forecasting total electron content (TEC)

Kosary, Mona; Forootan, Ehsan; Farzaneh, Saeed; Schumacher, Maike

Published in:
Journal of Geodesy

DOI (link to publication from Publisher):
10.1007/s00190-022-01623-y

Publication date:
2022

Document Version
Accepted author manuscript, peer reviewed version

Link to publication from Aalborg University

Citation for published version (APA):
Kosary, M., Forootan, E., Farzaneh, S., & Schumacher, M. (2022). A sequential calibration approach based on the ensemble Kalman filter (C-EnKF) for forecasting total electron content (TEC). *Journal of Geodesy*, *96*(4), Article 29. https://doi.org/10.1007/s00190-022-01623-y

General rights
Copyright and moral rights for the publications made accessible in the public portal are retained by the authors and/or other copyright owners and it is a condition of accessing publications that users recognise and abide by the legal requirements associated with these rights.

- Users may download and print one copy of any publication from the public portal for the purpose of private study or research.
- You may not further distribute the material or use it for any profit-making activity or commercial gain
- You may freely distribute the URL identifying the publication in the public portal -

Take down policy
If you believe that this document breaches copyright please contact us at vbn@aub.aau.dk providing details, and we will remove access to the work immediately and investigate your claim.

Aalborg Universitet

A sequential calibration approach based on the ensemble Kalman filter (C-EnKF) for forecasting total electron content (TEC)

Kosary, Mona; Forootan, Ehsan; Farzaneh, Saeed; Schumacher, Maike

Published in:
Journal of Geodesy

DOI (link to publication from Publisher):
10.1007/s00190-022-01623-y

Publication date:
2022

Document Version
Accepted author manuscript, peer reviewed version

Link to publication from Aalborg University

Citation for published version (APA):
Kosary, M., Forootan, E., Farzaneh, S., & Schumacher, M. (2022). A sequential calibration approach based on the ensemble Kalman filter (C-EnKF) for forecasting total electron content (TEC). *Journal of Geodesy*, *96*(4), Article 29. https://doi.org/10.1007/s00190-022-01623-y

General rights
Copyright and moral rights for the publications made accessible in the public portal are retained by the authors and/or other copyright owners and it is a condition of accessing publications that users recognise and abide by the legal requirements associated with these rights.

- Users may download and print one copy of any publication from the public portal for the purpose of private study or research.
- You may not further distribute the material or use it for any profit-making activity or commercial gain
- You may freely distribute the URL identifying the publication in the public portal -

Take down policy
If you believe that this document breaches copyright please contact us at vbn@aub.aau.dk providing details, and we will remove access to the work immediately and investigate your claim.

Journal of Geodesy manuscript No.
(will be inserted by the editor)

A sequential Calibration approach based on the Ensemble Kalman Filter (C-EnKF) for forecasting Total Electron Content (TEC)

M. Kosary, · E. Forootan, · S. Farzaneh, · M. Schumacher

Received: date / Accepted: date

Abstract Ionospheric models are applied for computing the Total Electron Content (TEC) in ionosphere to reduce its effects on the Global Navigation Satellite System (GNSS)-based Standard Point Positioning (SPP) applications. However, the accuracy of these models is limited due to the simplified model structures and their dependency on the calibration period. In this study, we present a sequential Calibration approach based on the Ensemble Kalman Filter (C-EnKF) to improve TEC estimations. Its advantage, over the frequently implemented state-of-the-art, is that a short period of GNSS network measurements is needed to calibrate model parameters. To demonstrate the results, the International Reference Ionosphere (IRI)-2016 model is used as reference and the Vertical TEC (VTEC) estimates from 53 IGS stations in Europe are applied as observation. The C-EnKF is applied to calibrate four selected model parameters (i.e., IG_{12}, $URSI(771)$, $URSI(1327)$ and $URSI(1752)$ related to the ionospheric activity as well as height and density peak-modelling in the F2 layer), which are identified by performing a sensitivity analysis. The calibrated model, called 'C-EnKF-IRI', is localized within Europe and can be used for near-real time TEC estimations and forecasting of the next day (at least). Validation against the dual frequency GNSS measurements of three

M. Kosary
School of Surveying and Geospatial Engineering, College of Engineering, University of Tehran, Tehran 113654563, Iran
E-mail: mona.kosary@ ut.ac.ir

E. Forootan
Geodesy Group, Department of Planning, Aalborg University, Rendburggade 14, 9000, Denmark
E-mail: efo@plan.aau.dk

S. Farzaneh
School of Surveying and Geospatial Engineering, College of Engineering, University of Tehran, Tehran 113654563, Iran
E-mail: farzaneh@ ut.ac.ir

M. Schumacher
Geodesy Group, Department of Planning, Aalborg University, Rendburggade 14, 9000, Denmark
E-mail: maikes@plan.aau.dk

This version of the article has been accepted for publication, after peer review (when applicable) and is subject to Springer Nature's AM terms of use, but is not the Version of Record and does not reflect post-acceptance improvements, or any corrections. Final version: https://link.springer.com/article/10.1007/s00190-022-01623-y#citeas
Citations: Kosary, M., Forootan, E., Farzaneh, S., Schumacher, M. A sequential calibration approach based on the ensemble Kalman filter (C-EnKF) for forecasting total electron content (TEC). J Geod 96, 29 (2022). https://doi.org/10.1007/s00190-022-01623-y

IGS stations indicates that during September 2017, the accuracy of forecasting VTECs is improved up to 64.87% compared to IRI-2016. The electron density (Ne) profiles of C-EnKF-IRI are validated against those of COSMIC products, which indicates ∼38.1% improvement during days with low ($Kp = 3$) and high ($Kp = 8$) geomagnetic activity. Applying the forecasts of VTECs in SPP experiments shows similar performance as the 11-days delayed IONEX data, i.e., 51%, 52% and 79%, improvements in estimating ionospheric contributions compared to the usage of the original IRI-2016, Klobuchar and NeQuick-G models, respectively. The TEC forecasts of C-EnKF-IRI are found to be of the same quality of the IONEX final TEC products in SPP applications.

Keywords Sequential Calibration · Ensemble Kalman Filter (EnKF) · International Reference Ionosphere (IRI) · GNSS · Standard Point Positioning (SPP) · Total Electron Content (TEC) · Vertical TEC (VTEC)

1 Introduction

The rapid development of space-geodetic observation techniques has brought out a wide range of applications such as positioning and navigation. In fact, the Global Navigation Satellite System (GNSS, *Mulassano et al.*, 2004) technique has become an integral part of applications, where mobility plays an important role. Standalone GNSS signals enable the calculation of unknown positions using information transmitted by various constellations. However, given the high orbital altitude (around 20000-35000 km) and high speed of satellites, these position estimates contain errors, e.g., ($\sim 4m$) using ordinary corrections (*Verhagen et al.*, 2010). Such big uncertainties would not meet the requirements of emerging applications such as drones, augmented reality and autonomous vehicles demanding for 'high accuracy ($< 1m$) and precision', as well as 'real-time' positioning in the mass-market.

To improve the accuracy of GNSS positioning, several signal augmentation techniques such as the Real Time Kinematic (RTK, *Boulic et al.*, 1990) and Differential GNSS (DGNSS, *Groves*, 2015), as well as the process-based technique of Precise Point Positioning (PPP, *Zumberge et al.*, 1997) or the hybrid variations (e.g., PPP-RTK, *Wübbena et al.*, 2005) have been developed. These technologies are able to deliver cm/dm level accuracy, but they need corrections to eliminate main errors of the code-derived pseudo-range and carrier phase measurements including clock biases, ionospheric and tropospheric effects, relativity, and receiver/satellite instrumental biases. In this study, we focus on the estimation of ionospheric effects, which needs to be applied on single frequency measurements of the Standard Point Positioning (SPP) applications.

The signals of GNSS must transit the ionosphere (i.e., part of atmosphere around 60 km up to around 2000 km, containing ionized plasma of different gas components) on their way to receivers (*Kelley*, 2009; *Kursinski et al.*, 1997). The interactions between these signals and the Total Electron Content (TEC) within the ionosphere (*Kedar et al.*, 2003) lead to signal bending, adding delays on the code-derived pseudo-range and advancing the career phase measurements (*Dubey et al.*, 2006). Ionospheric effects, due to TEC changes, vary between 3 m and 15 m during the daytime and night time, e.g., for the GNSS L-band (1 GHz-2

GHz) signals (*Wu et al.*, 2013; *Yuan and Ou*, 2001b). During high solar activity (demonstrated by the magnetic activity index $Kp > 6$), the ionospheric effect might reach up to 40 m and 100 m in the vertical and the line-of-sight signal propagation direction, respectively (*Wu et al.*, 2013; *Yuan and Ou*, 2001a).

To achieve high accuracy in GNSS positioning and navigation applications, the effects of ionosphere is tried to be eliminated (*Goncharenko et al.*, 2013). According to the dispersed properties of the ionosphere, dual-frequency GNSS users can estimate the first-order ionosphere effect by linear combinations of the measurements. However, this method cannot be performed for the single frequency receivers (most of SPP applications, *Øvstedal*, 2002), where the ionosphere impact on signal propagation has to be mitigated by applying corrections from models. In the PPP applications, providing an accurate and fast estimation of TEC can improve the positioning accuracy, and decreases its convergence time (*Sanz Subirana et al.*, 2013; *Rose et al.*, 2014; *Rovira-Garcia et al.*, 2015; *Su et al.*, 2019a; *Zhang et al.*, 2020).

The ionospheric correction models, which can be used for simulating and forecasting TECs and their equivalent effects, are categorized into three main types (*Jakowski et al.*, 2011): (1) Broadcast Ionospheric Models (BIMs) such as the Klobuchar, NeQuick-Gal and BeiDou Global Ionospheric Model (BDGIM) (*Yuan et al.*, 2019; *ICD*, 2017a,b, 2020); (2) Empirical Ionospheric Models (EIMs) such as the International Reference Ionosphere (IRI, *Bilitza*, 2001) and the Parameterized Ionospheric Model (PIM, *Daniell et al.*, 1995); and (3) the data-driven models such as the Global Ionospheric Maps (GIMs) produced by the International GNSS Service (IGS), Ionospheric Analysis Associate Centers (IAACs, *Andersen et al.*, 2010), and research institutes (e.g., *Farzaneh and Forootan*, 2018; *Goss et al.*, 2020).

The simulation and forecasting skills of existing models (e.g., categorized in 1 and 2) are limited due to the simplified model structures and model sensitivity to the calibration period (*Jee et al.*, 2010). Though these models are very useful for providing TEC estimations in real-time applications, such as the Neustrelitz TEC Model (NTCM) proposed by (*Hoque et al.*, 2020) to be used for Galileo. The accurate data-driven TEC models (in 3) are often unavailable in real-time. For example, the final Global Ionospheric Map (GIM), provided by the Center for Orbit Determination in Europe (CODE), are available with 11 days delay (*Johnston et al.*, 2017) and their spatial and temporal resolutions are limited, i.e., the CODE-GIM is delivered every hour in terms of spherical harmonics of up to degree and order 15 or in girds of $2.5^\circ \times 5^\circ$ in latitude and longitude, respectively (*Schaer et al.*, 1996b; *Schaer and helvétique des sciences naturelles. Commission géodésique*, 1999). Therefore, most of the previous studies addressed improving the modelling of TECs either through empirical corrections (e.g., *Borries et al.*, 2007; *Yuan et al.*, 2008a,b; *Bouya et al.*, 2010; *Mukhtarov et al.*, 2013; *Li et al.*, 2015; *Farzaneh and Forootan*, 2020) or statistical data-model integration, e.g., (*Spalla and Cairolo*, 1994; *Katamzi et al.*, 2012; *Wan et al.*, 2012; *Li and Guo*, 2010), as well as Kalman Filter (KF) based predictions (e.g., *Bust et al.*, 2004; *Schunk et al.*, 2004; *Scherliess et al.*, 2004; *Erdogan et al.*, 2020).

The adopted methodology of this study is close to those who apply ensemble based integration techniques, where examples include *He et al.* (2020) who integrated GNSS-derived TEC measurements in Thermosphere-Ionosphere-Electrodynamics General Circulation Model (TIEGCM) and showed that the forecasting accuracy of TEC estimates can be improved by at least 10% for 24 hr. *An et al.* (2020) followed a similar approach to reduce biases in the International Reference Ionosphere (IRI) model (*Bilitza*, 2018). *Mengist et al.* (2019) applied the 4-D assimilation technique (*Bust and Datta-Barua*, 2014) to localize an ionosphere model, based on IRI-2016, over Korea and adjacent areas. They demonstrated that the new IDA4D model provides TEC estimates that contain 17% less bias compared to the original model.

In this study, we introduce a sequential Calibration technique based on the Ensemble Kalman Filter (EnKF, *Evensen*, 2003; *Schumacher*, 2016), thus, the method is abbreviated as 'C-EnKF'. As observation, TEC estimates of a regional GNSS network are applied to calibrate selected parameters of IRI-2016. After performing the calibration, the model is called 'C-EnKF-IRI', which is localized over the region of interest, and it is believed to be better fitted for forecasting Vertical TECs (VTECs) in the next day. Our argument is that the newly calibrated model parameters are fitted against the recent TEC estimates, thus, it is likely that they can better reflect the evolution of ionosphere (compared to the original model parameters that are computed during older periods with another physical conditions).

Our motivation to select IRI-2016 as the basis of integration is due to its ability to describe the physical properties of the ionosphere, and its simple structure. Our goal is to show that the model's known limitations in simulating VTEC during the periods with different solar activities can be improved by calibrating the model against the VTEC observations from a regional GNSS network. In theory, the presented approach of this study is generic, thus, IRI-2016 can be replaced by another arbitrary model.

The IGS network in Europe is considered here to perform the estimation, where 56 freely available stations with an average between-station distance of ~ 70 km to 780 km (i.e., these values are respectively estimated as mean and median of minimum distance between stations) are used in this study to emphasize the fact that the network must not be very dense to achieve regional improvements. Please note that commercial correction networks, such as SAPOS (in Germany), and FLEPOS (in the Netherlands) contain more homogeneously distributed stations and their density is relatively higher, i.e., ~ 50 km and 30 km, respectively (*Engfeldt*, 2005). Thus, localizing available models using the freely available IGS stations with similar performance of the commercial networks, i.e., forecasting with the accuracy of 1-2 TEC Unit (TECU), is desirable for GNSS, e.g., SPP, applications.

We formulated the C-EnKF, instead of using ordinary calibration techniques, because it can calibrate the most sensitive model parameters without linearizing the model unlike what Least Squares (LS) techniques would need (see, e.g., *Krypiak-Gregorczyk et al.*, 2017). The C-EnKF also uses the GNSS observations, when they are available, therefore existing gaps in the measurements do not affect the entire calibration procedure. The calibrated parameters, which are estimated by C-EnKF, are then applied to estimate VTECs in areas that are not covered by the IGS network and to forecast VTECs in future.

C-EnKF is different from most of the previous studies, where their focus is on the 'data assimilation' that only updates the model states, e.g., (V)TECs, using observations. Even though, some interesting applications have been shown in forecasting (V)TECs (e.g., *Wu et al.*, 2015), those predictions only took advantage of the updated model states (i.e., a better initialization for forecasting). In this study, however, we will present the possibility of 'calibrating' the model's parameters, which is likely more efficient (than the data assimilation technique) for forecasting VTECs.

To numerically implement the C-EnKF, 56 IGS stations within Europe are used. For estimating VTEC, we only processed the dual frequency signals of the GPS constellation because of its consistency within the all available IGS measurements. At first, the GPS signals (phase and code measurements) are applied to estimate VTECs at a single layer with the height of 450 km. Then, the VTEC estimates of 53 stations are used in C-EnKF to calibrate selected key parameters that are derived by applying a sensitivity analysis of the IRI-2016 model. Finally, the VTEC forecasts of C-EnKF-IRI are validated against the VTECs derived from dual frequency measurements of three stations that were not used during the calibration procedure. The independent validations are also performed against the electron density (Ne) profile of C-EnKF-IRI with those of COSMIC (e.g., *Liou et al.*, 2007) and critical frequency in the F2 ($foF2$) with those of in-situ ionosonde stations during days with low and high geomagnetic activity. Finally, TEC estimates of C-EnKF-IRI are compared with the output of Klobuchar, the original IRI-2016, NeQuick and GIM models in the SPP mode to assess their performance in computing ionospheric corrections for such positioning applications.

This paper is organized as follows: the data and model sources are described in Section 2, followed by the methodology of sensitivity analysis. C-EnKF, and the evaluation measures used in this study being presented in Section 3. The numerical results, including the forecasts of VTEC values in Europe and validations are provided in Section 4. Finally, this study is concluded in Section 5.

2 Data and Models

To introduce the VTEC observations, GPS measurements of 56 IGS stations within Europe (Fig. (1)) are obtained from `ftp://cddis.gsfc.nasa.gov/` with 30-second sampling rate covering the entire September 2017. The raw data can be downloaded as the Receiver Independent Exchange (RINEX) format. Measurements of the three IGS stations, selected to be GRAZ (longitude: 15.493°E and latitude: 47.067°N in Austria), PTBB (longitude: 10.460°E and latitude: 52.296°N in Germany), and M0SE (longitude: 12.493°E and latitude: 41.893°N in Italy (purple dots in Fig. (1)) are not considered during the calibration period, but they are used for evaluating the forecasting performance of C-EnKF-IRI.

In what follows, the procedure to estimate GNSS-derived VTEC values and their uncertainties is described in Section 2.1. Details of IRI-2016 and other models are provided in Sections 2.2 and 2.3.

2.1 VTEC Determination from Dual Frequency GPS Measurements

The ionospheric effect on the pseudo-range I_i for the signal frequency f and the Slant Total Electron Content (STEC) estimates can be derived by analyzing differential code and carrier phase measurements of the dual frequency GPS L1 and L2. Estimating STECs from code measurements is straightforward, however, it contains considerable noise level, which needs to be treated. The STEC estimates

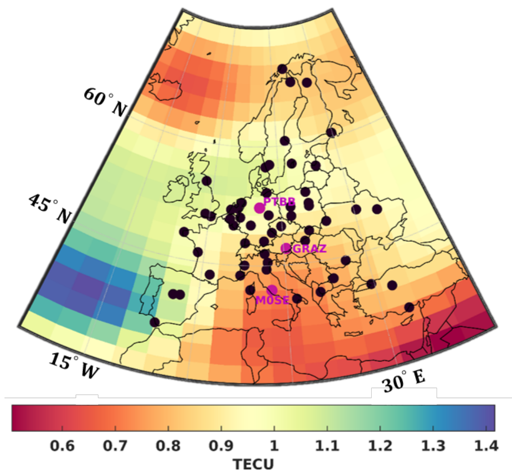

Fig. 1: An overview of the 56 IGS stations within Europe. From these, GPS measurements of 53 stations (shown in black) are used in the C-EnKF procedure to estimate VTEC values that are introduced as observation during the calibration period. VTECs of the three stations (in purple), corresponding to GRAZ, M0SE, and PTBB, are used for validation. The gridded mean of Root Mean Squares (RMS) of VTECs derived from the CODE-GIM model during September 2017 is shown as background map.

from the carrier phase measurements contain lower noise level (compared to code), however, the ambiguity number will present in the differential equations (*Zhang et al.*, 2019). In order to derive smooth and ambiguity-independent STECs (in TECU, i.e., TECU= $10^{16} el/m^2$), the 'carrier to code leveling process' method as in *Nohutcu et al.* (2010), is implemented, i.e.,

$$I_i = \pm \frac{40.3}{f^2} \text{STEC}, \tag{1}$$

$$\text{STEC} = (\tilde{P}_4 - br - bs - \langle \varepsilon_p \rangle_{arc} + \varepsilon_L) \left(\frac{f_1^2 f_2^2}{40.3(f_2^2 - f_1^2)} \right), \tag{2}$$

where $\tilde{P}_4$ is the pseudo-range ionospheric observable smoothed by the carrier-phase ionospheric one, i.e.,

$$\tilde{P}_4 = \langle P_4 + \Phi_4 \rangle_{arc} - \Phi_4 \approx I_1 - I_2 + br + bs + \langle \varepsilon_p \rangle_{arc} - \varepsilon_L. \tag{3}$$

In Eqs. (2) and (3), P_4 and Φ_4 are the geometry-free linear combination of pseudo-range and carrier phase measurements in the continuous observational arc, I_1 and I_2 are the ionospheric refraction delays at L1 and L2, br and bs are the code inter-frequency biases (IFBs) for the receiver, and f_1 and f_2 are the L_1 (1575.420 MHz) and L_2 (1227.600 MHz) frequencies. Finally, ε_p and ε_l are the effects of multi-path and measurement noise on the pseudo-range and carrier phase, respectively.

Since IRI-2016 simulates the VTEC values, the STECs in Eq. (2) are transformed into the height-independent VTEC estimates using the Single-Layer Model (SLM) mapping function (*Schaer et al.*, 1996a) as:

$$\text{VTEC} = \frac{\text{STEC}}{\text{MF}}, \tag{4}$$

with

$$\text{MF} = \frac{1}{\cos z'}, \qquad \sin z' = \frac{R_E}{R_E + H} \sin z, \tag{5}$$

where R_E is the Earth's mean radius (i.e., 6378.1363 km), z and z' are the zenith angles of the satellite at the user position and the ionospheric pierce point, and H is the mean altitude that is considered here to be 450 km to be consistent with the IONEX estimates (see Section. 2.3).

To estimate the uncertainties of VTEC estimates, being used in C-EnKF, we follow a variance propagation method as:

$$\sigma_{\text{GPS-VTEC}} = \frac{\alpha}{MF} \times \sqrt{\sigma^2_{\tilde{P}_4} + \sigma^2_{br} + \sigma^2_{bs}}, \tag{6}$$

$$\alpha = \frac{f_1^2 f_2^2}{40.3(f_2^2 - f_1^2)}, \tag{7}$$

while assuming that $\sigma_P = \sigma_{P_1} = \sigma_{P_2} = 0.2 \;\; m$ and $\sigma_\phi = \sigma_{\phi_1} = \sigma_{\phi_2} = 0.02 \;\; cycle$, and the code pseudo-range and carrier phase derived TECs are treated to be uncorrelated. The uncertainty of $\tilde{P}_4$ (in Eq. (3)) can be estimated as:

$$\sigma^2_{\tilde{P}_4} = \sigma^2_\phi \times \lambda_1^2 + \sigma^2_\phi \times \lambda_2^2 + \frac{1}{n}(\sigma^2_\phi \times \lambda_1^2 + \sigma^2_\phi \times \lambda_2^2 + 2 \times \sigma^2_P), \tag{8}$$

where λ_1 and λ_2 correspond to the wavelength of carrier phase (i.e., 19.03 cm and 24.42 cm), n is the number of measurements in the continuous arc, and σ_{br} and σ_{bs} can be replaced by those from the Differential Code Bias (DCB) files provided by the University of Bern (`http://ftp.aiub.unibe.ch/BSWUSER52/ORB/`).

2.2 International Reference Ionosphere 2016 (IRI-2016)

IRI-2016 is a standard model for the specification of plasma parameters in the Earth's ionosphere, which is developed by the Committee on Space Research (COSPAR) and the International Union of Radio Science (URSI, *Rawer et al.*, 1978). Similar to other empirical models, IRI-2016 uses most of the available data sources for improving the simulation of ionosphere properties (e.g., ionosonde, incoherent scatter radar, in-situ, and satellite measurements *Bilitza*, 2018). Electron density, electron temperature, ion temperature, ion composition, as well as VTEC estimates can be simulated by IRI-2016 for the altitude range between 50 km-2000 km based on the geodetic latitude (φ) and longitude (λ), Local apparent Solar Time (LST), solar index ($F_{10.7}$, *Tapping*, 2013) or (R_{12}, *Reinisch et al.*, 2013), magnetic index (Ap, *Ahluwalia*, 2000), ionosphere index IG_{12}, and the model coefficients of URSI or CCIR that are used to force hourly-monthly variations of the F2 layer's critical frequencies ($foF2$, *Rishbeth*, 1998).

The variation of $foF2$ in mathematically represented by a combination of the Fourier expansion and the geographic functions to account for temporal and spatial changes, respectively (*Union-Radiocommunication*, 2009). For this, the $foF2$

values are extracted by analyzing the ionosond measurements from stations around the world. *Pignalberi* (2019) states that 13 Fourier coefficients and the geographic function up to the order of 76 are currently used in IRI-2016. Thus, IRI-2016 needs $13 \times 76 = 988$ coefficients to globally model the $foF2$ but this is done for two selected levels of solar activity, i.e., ($IG_{12} = 0$ and $IG_{12} = 100$). Therefore, the total number of monthly stored coefficients is 988 $\times$ 2 levels of solar activity = 1976 coefficients (*Reinisch et al.*, 2013).

In IRI-2016, the global maps of the height and density peaks in the F2 layer, which are shown by HmF2 and NmF2, respectively, are determined based on the $foF2$ and they are introduced by considering the International Radio Consultative Committee model (*CCIR*, 1967) and the International Union of Radio Science (URSI, *Jones and Gallet*, 1962). Between CCIR and URSI, the latter is recommended to model $foF2$ because it applies an ionospheric condition-dependent method to interpolate gaps in global maps and the number of measurements to tune URSI is more than that of CCIR (*Brown et al.*, 2018b).

IRI-2016 accepts the 12-month running mean of the solar index R (denoted R_{12}) due to the higher correlation between R_{12} and ionosonde-measured $foF2$ than that between the daily R and $foF2$. In addition to R_{12}, the daily solar radio flux ($F_{10.7}$) from `ftp://ftp.ngdc.noaa.gov` is used instead of the sunspot number to represent the variations of solar activity. The daily $F_{10.7}$ is temporally smoothed to produce 81-day and 365-day averages, where the first is utilized for estimating the topside electron temperature and the ion composition and the latter is used for relative density estimation of the molecular and atomic ions. The Ap and Kp indexes represent the general level of geomagnetic activity with the temporal sampling of 3 hours (*Webb and Howard*, 1994). Since Kp is quasi-logarithmic local index of the 3-hourly range in magnetic activity, it is not meaningful to take the average of a set of Kp indices during a day. Therefore, 3-hour Kp index are converted into a linear scale called the Ap index (*Allen*, 2004). The Ap index (`ftp://ftp.ngdc.noaa.gov/STP/GEOMAGNETIC_DATA/INDICES/KP_AP`) and R_{12} (`ftp://ftp.ngdc.noaa.gov/STP/SOLAR_DATA/`) are introduced to determine the electron density in IRI-2016. Another index is the Ionosonde Global (IG_{12}), which proposed by *Liu et al.* (1983) and represents some additional ionospheric changes due to solar activity in the F region (*Bilitza et al.*, 2017). This index is computed based on modifying the 12-month running mean of the sunspot number R_{12} to make the foF2 measurements of some selected ionosonde stations consistent with values from the CCIR foF2 model (*Liu et al.*, 1983; *Brown et al.*, 2018a; *Liu et al.*, 2019).

2.3 Ionospheric Models for Comparisons

TEC estimates from the Klobuchar, NeQuick and the IONEX models are used in this study to evaluate the results of the original IRI-2016 and its calibrated version, i.e., C-EnKF-IRI. The Klobuchar model (*Klobuchar*, 1987) has been applied by the GPS navigation users to mitigate the effect of ionospheric delay because of its simple computation and minimum number of coefficients.

NeQuick contains six semi-Epstein layers with modeled thickness parameters for 'quick' ionospheric electron density and TEC computation in trans-ionospheric propagation applications. This model is adopted for providing ionospheric corrections in the single frequency operation of Galileo constellation (*Nava et al.*, 2008; *Aragon-Angel et al.*, 2019). Recently, the BeiDou Global Ionospheric Model (BDGIM) has been developed (*Yuan et al.*, 2019; *ICD*, 2017a,b, 2020), whose outputs will be used in future for validation.

Since 1998, the International GNSS Service (IGS) associates analysis centers have established products containing VTEC maps derived from the dual-frequency GNSS data in IONEX (IONosphere EXchange) format. IONEX produces VTEC with a spatial resolution of $2.5^\circ \times 5^\circ$ in latitude and longitude, respectively, and a temporal resolution of few minutes to several hours in rapid and final modes. These products are available with a latency of less than 24 hours and approximately 11 days in the rapid and final solution modes, respectively (*Feltens and Schaer*, 1998; *Hernández-Pajares et al.*, 2009).

3 Method

C-EnKF can be used to calibrate selected model parameters. To define these parameters, the Global Sensitivity Analysis (GSA, *Saltelli*, 2002b) is applied on IRI-2016, which is discussed in 3.1. The mathematical formulation of C-EnKF is presented in 3.2.

3.1 Global Sensitivity Analysis (GSA)

To identify key parameters that dominantly contribute in producing model outputs (here VTECs of IRI-2016), the GSA (*Saltelli*, 2002a) is implemented, which is necessary because it increases efficiency of calibration by introducing the updates to the most important parameters. Among the GSA algorithms, that of Sobol (*Sobol*, 1990), which is a variance-based approach and works effectively for non-linear models, is used in this study. We apply Sobol's sensitivity index to compute the contribution of each parameter to the overall variance while considering the interactions with other parameters (*Sobol*, 1990; *Saltelli*, 2002a; *Forootan et al.*, 2020).

Parameters are selected to be the geodetic latitude (φ) and longitude (λ), solar flux ($F_{10.7}$) and its three-month average ($F_{10.7A}$), 12-month smoothed ionospheric activity index (IG_{12}) and the sunspot number (R_{12}), as well as model coefficients including the URSI that contains 1976 elements. To describe the Sobol method, the IRI-2016 model (*Bilitza*, 2018) is presented in the functional form as:

$$\mathrm{Y} = F(X_1, \cdots, X_p) = F(\varphi, \lambda, F_{10.7}, F_{10.7A}, IG_{12}, R_{12}, URSI_{1,\cdots,1976}), \qquad (9)$$

where Y represents the VTEC estimates of the model, $\mathrm{X} = (X_1, \cdots, X_p)$ stand for a set of p model parameters (here p is 1982=6+1976).

The first order Sobol's sensitivity indices S_i are computed using:

$$\text{Sensitivity index} : S_i = \frac{D_i}{D}, \qquad (10)$$

where the partial variance D_i represents a portion of the total variance D.

Because IRI-2016 is non-linear, it is almost impossible to calculate the variances of individual parameters analytically (*Nossent et al.*, 2011). Hence, the Monte

Carlo sampling approach of (*Gan et al.*, 2014) is considered here following the implementation in *Saltelli et al.* (2010). For this, we consider two $n \times p$ independent matrices of **A** and **B**, where n is the ensemble size and p represents the number of parameters. Entries of these matrices are filled by generating 90 ensembles of the parameters considered in Eq. (9) using the Gaussian distribution with the mean value equal to the default value of the parameters and its standard deviation to be 1% of the default value. The variances in Eq. (10) can be numerically evaluated as (see also, *Sobol*, 2001; *Zhang et al.*, 2013):

$$\mathrm{D} = \frac{1}{2n-1} \sum_{s=1}^{n} [F^2(X_{A1}, \ldots, X_{Ap}) + F^2(X_{B1}, \ldots, X_{Bp})] - F_0^2, \tag{11}$$

where n is the ensemble size, $F(X_{A1}, \ldots, X_{Ap})$ and $F(X_{B1}, \ldots, X_{Bp})$ are the model output evaluated against the ensemble model's input A and B, respectively, and F_0 is the expected value of the model output that is estimated using:

$$F_0^2 = \frac{1}{n} \sum_{s=1}^{n} F(X_{A1}, \ldots, X_{Ap}) \times F(X_{B1}, \ldots, X_{Bp}). \tag{12}$$

Partial variances in Eq. (10) that are related to the parameters X_i are computed as:

$$D_i = \frac{1}{2n-1} \sum_{s=1}^{n} [F(X_{A1}, \ldots, X_{Ap}) \times F(X_{B1}, \ldots, X_{B(i-1)}, X_{Ai}, X_{B(i+1)}, \ldots, X_{Bp})] - F_0^2. \tag{13}$$

where each $F(X_{B1}, \ldots, X_{B(i-1)}, X_{Ai}, X_{B(i+1)}, \ldots, X_{Bp})$ is the IRI-2016 model output whose parameters are taken from the sample matrix B, except X_i, which takes the inputs from A.

3.2 Sequential Calibration Based on the Ensemble Kalman Filter (C-EnKF)

Core of the calibration procedure is selected to be the EnKF (as in *Evensen*, 2009; *Schumacher*, 2016; *Forootan et al.*, 2020). This technique uses the available measurements sequentially and based on their error covariance and those of model, then it decides how to update (calibrate) the model's parameters. To formulate the calibration procedure in a general way, let us assume that the original model of Eq. (9) is rewritten as:

$$\text{Original model, e.g., IRI-2016} : F(\Theta) = F(\Theta_0, \Theta_R, \Theta_I), \tag{14}$$

where Θ is a vector of parameters and input values in the model. In our formulation, we consider that Θ consists of $\Theta_{0_{m_1 \times 1}}$ that are the key parameters from GSA (Sec. 3.1) and will be updated during the calibration procedure, Θ_R represents those parameters that will remain unchanged during calibration, and Θ_I indicates the input variables such as the solar and geomagnetic indices, location, and time.

Ensembles of the model's key parameters are generated by a Monte Carlo simulation that considers i^{th} (i.e., $i = 1, ...n$) ensemble members of the key parameters ($\mathbf{X}^f_{1,i}$) expressed as:

$$\mathbf{X}^f_{1,i} = \Theta_0 + \xi_i,\ i = 1, ...n, \tag{15}$$

where $\Theta_{0_{m_1\times 1}}$ is a vector of default values of the key parameters in IRI-2016 as in Eq. (14) plus random errors (ξ_i) that perturb these initial values. Similar to GSA (Sec. 3.1) , the magnitude of noise is decided to be 1% of each variable. The four most sensitive parameters ($m_1 = 4$) from GSA are considered here to be calibrated using the VTEC measurements. In the C-EnKF procedure, ensembles of 90 members ($n = 90$) are used to perform the numerical integration. The GNSS-derived VTECs are obtained from 53 IGS stations within Europe, which makes it $m_2 = 53$ observations in each epoch to be used for calibration.

The ensemble of key parameters ($\mathbf{X}^f_1$) and model states (i.e., simulated VTECs using perturbed key parameters ($\mathbf{X}^f_2 = F(\Theta_0 + \xi, \Theta_R, \Theta_I)$) are integrated and denoted by $\mathbf{X}_{m\times n}$ as:

$$\mathbf{X}^f = \begin{bmatrix} \mathbf{X}^f_{1\,m_1\times n} \\ ------ \\ \mathbf{X}^f_{2\,m_2\times n} \end{bmatrix}, \tag{16}$$

where the upper-index 'f' represents the model forecast. The ensemble mean vector ($\bar{\mathbf{x}}^f_{m\times 1}$) of Eq. (16) and the covariance matrix of the forecasting step ($\mathbf{C}^f_{m\times m}$) are defined as:

$$\bar{\mathbf{x}}^f = \begin{bmatrix} \bar{\mathbf{x}}^f_1 \\ \bar{\mathbf{x}}^f_2 \end{bmatrix}, (e.g.,\ \bar{\mathbf{x}}^f_1 = \frac{1}{n}\sum_{i=1}^{n} \mathbf{x}^f_{1,i}), \tag{17}$$

$$\mathbf{C}^f = \frac{1}{n-1}(\mathbf{X}^f - \bar{\mathbf{x}}^f)(\mathbf{X}^f - \bar{\mathbf{x}}^f)^T, \tag{18}$$

In each analysis step, shown by the upper-index 'a', the estimation of key parameters ($\mathbf{X}^a$) follows:

$$\mathbf{X}^a_{m_1\times n} = \mathbf{X}^f_1 + \mathbf{K}_\Theta(\mathbf{Y} - \mathbf{H}\mathbf{X}^{\mathrm{f}}), \tag{19}$$

and their ensemble mean, shown by $\bar{\mathbf{x}}^a$, is computed as:

$$\bar{\mathbf{x}}^a_{m_1\times 1} = \bar{\mathbf{x}}^f_1 + \mathbf{K}_\Theta(\bar{\mathbf{y}} - \mathbf{H}\bar{\mathbf{x}}^f), \tag{20}$$

Here, $\mathrm{Y}_{m_2\times n}$ and $\bar{\mathbf{y}}_{m_2\times 1}$ represent the ensembles (i.e., perturbed by the estimated noise from Eq.6) and the ensemble mean of GNSS VTECs, respectively. Therefore, according to Eqs. (19 and 20), the estimated updates directly depend on the differences between the real observations (Y) and model predictions ($\mathbf{H}\mathbf{X}^{\mathrm{f}}$), while considering their weights, which are reflected in the Kalman gain matrix ($\mathbf{K}_{\Theta\,m_1\times m_2}$) that is computed as:

$$\mathbf{K}_\Theta = \mathbf{C}^{\mathrm{f}}_\Theta \mathbf{H}^{\mathrm{T}} \left(\mathbf{H}\mathbf{C}^{\mathrm{f}}\mathbf{H}^{\mathrm{T}} + \mathbf{C}^{\mathrm{R}}\right)^{-1}, \tag{21}$$

In Eq. (21), the cross covariances between the key parameters and the state variables are represented by $\mathbf{C}^f_{\Theta m_1 \times m_2}$, i.e.,:

$$\mathbf{C}^f_{\Theta m_1 \times m_2} = \frac{1}{n-1}(\mathbf{X}^f_1 - \bar{\mathbf{x}}^f_1)(\mathbf{X}^f_2 - \bar{\mathbf{x}}^f_2)^T, \tag{22}$$

where $\mathbf{X}^f_1$ and $\mathbf{X}^f_2$ are defined as the ensemble of key parameters and model state, and $\bar{\mathbf{x}}^f_2$ and $\bar{\mathbf{x}}^f_1$ are the ensemble mean of key parameters and model state, respectively.

The covariance matrix of GNSS-derived VTEC observations is shown by $(\mathrm{C}^{\mathrm{R}}_{m_2 \times m_2})$. Assuming that the measurements of each GNSS station to be independent, it will be diagonal matrix whose the estimations follows:

$$\mathbf{C}^{\mathrm{R}}_{m_2 \times m_2} = diag(\sigma^2_{\text{GNSS-VTEC}_i}), (i = 1, \cdots, m_2) \tag{23}$$

where the root of its diagonal elements is determined by Eq. (6). In Eqs. (19, 20, and 21), the design matrix $\mathbf{H}$ is defied as:

$$\mathbf{H}_{m_2 \times m} = [\mathbf{0}_{m_2 \times m_1} \;\; \mathbf{I}_{m_2 \times m_2}], \tag{24}$$

where $\mathbf{0}_{m_2 \times m_1}$ is a zero matrix, and $\mathbf{I}_{m_2 \times m_2}$ represents the identity matrix. This means that in each step of the Kalman Filter process observations have a linear relationship with the model states.

C-EnKF procedure (Eq. 16 to Eq. 24) has been evaluated at each time step to obtain the ensemble of parameters (i.e, $\mathbf{X}^a$), and their mean (i.e, $\bar{\mathbf{x}}^a$). The ensemble of key parameters from analysis step (Eq. (19)) is used for the forecasting step ($\mathbf{X}^f_1$ of Eq. (16)) of the next time step in simulating VTEC values and the calibration procedure continues until the observations are accessible.

The calibration procedure is performed using 24 hours of GNSS VTEC estimates. The last set of parameters that are estimated by Eq. (20) are considered as the optimal solution, which provides us with $\hat{\Theta}_0$. These parameters then replace the default values of the original IRI-2016 model Eq. (14) to estimate those VTECs that are not covered by IGS station or for forecasting the VTECs for the next day (covering the entire Europe). The (daily) calibrated model is known here as 'C-EnKF-IRI', which can be represented by:

$$\text{Calibrated model, i.e., } : \mathrm{F}(\hat{\Theta}_0, \Theta_R, \Theta_I), \tag{25}$$

The forecasting of VTECs for the next day can be evaluated using the predictor model as:

$$\text{Predictor model, i.e., } : \mathrm{F}(\hat{\Theta}_{0,d}, \Theta_R, \Theta_{I_{d+1}}), \tag{26}$$

where d is the day that C-EnKF is implemented. Thus, the predictor model can be run using the calibrated values of the day d, i.e., $\hat{\Theta}_{0,d}$, and the indices of the next day $d+1$, i.e., $\Theta_{I_{d+1}}$. Other parameters, i.e., Θ_R, remain unchanged. An overview of the C-EnKF procedure to calibrate IRI-2016 and its evaluation is shown in Fig. (2).

3.3 Evaluation Measures

To evaluate the performance of the original and calibrated models, the following metrics are applied.

- 'Bias' is defined as:

$$\text{Bias} = \frac{1}{n}\sum_{i=1}^{n}(\text{Obs}_i - \text{Model}_i), \quad (27)$$

  where Obs and Model denote observation and model estimates, receptively, and n is the number of observations.
- The expression of bias in percentage is determined based on the 'Relative Difference (RD)', which is computed as:

$$\text{RD} = 100 \times \sum_{i=1}^{n}(\frac{\text{Obs}_i - \text{Model}_i}{\text{Obs}_i}), \quad (28)$$

  where the positive (negative) values of the bias and RD results indicate that the model underestimates (overestimates) compared to the observations.
- 'Root Mean Squares of Error (RMSE)' is computed to show how well model estimates agree with observations as:

$$\text{RMSE} = \sqrt{\frac{\sum_{i=1}^{n}(\text{Obs}_i - \text{Model}_i)^2}{n}}. \quad (29)$$

  The square term inside the RMSE equation highlights both positive and negative differences between the quantities.
- 'Improvement' is defined as changes in the computed RMSEs after implementing C-EnKF as:

$$\text{Improvement} = 100 \times \frac{\text{RMSE}_1 - \text{RMSE}_2}{\text{RMSE}_1}, \quad (30)$$

  where RMSE_1 is computed using the original IRI-2016 and GNSS-derived VTECs, and RMSE_2 is determined using those of C-EnKF-IRI and GNSS-derived VTECs.
- 'Average of Absolute Percentage Deviation (AAPD)' is expressed as the percentage of absolute difference between observation and model as:

$$\text{AAPD} = 100 \times \frac{\sum_{i=1}^{n}(|\frac{\text{Obs}_i - \text{Model}_i}{\text{Obs}_i}|)}{n}, \quad (31)$$

  where $|.|$ computes the absolute values. Minimum (maximum) values of AAPD correspond to the average best (worst) performance of a model in estimating VTECs.
- 'Normalized Root Mean Square Error (NRMSE)' is used as a scale-independent measure to represent the fraction of the variance in the data that is predicted by the model, and it is defined as:

$$\text{NRMSE} = 1 - \frac{\sqrt{\sum_{i=1}^{n}(\text{Obs}_i - \text{Model}_i)^2}}{\sqrt{\sum_{i=1}^{n}(\text{Obs}_i - \bar{\text{Obs}})^2}}, \quad (32)$$

where $\bar{\text{Obs}}$ is defined as the mean of observations. In contrast to AAPD, the minimum (maximum) values of NRMSE correspond to the average worst (best) performance of model in simulating VTECs.

– 'Correlation Coefficients (CCs)' are used as a unit-less measure to represent the overall fit between model estimations and observations:

$$\text{CC} = \frac{\sum_{i=1}^{n} (\text{Model}_i - \bar{\text{Model}})(\text{Obs}_i - \bar{\text{Obs}})}{\sqrt{\sum_{i=1}^{n} (\text{Model}_i - \bar{\text{Model}})^2 \sum (\text{Obs}_i - \bar{\text{Obs}})^2}}. \tag{33}$$

The range of CCs is from −1 to +1, where −1 indicates the perfect negative correlation, +1 corresponds to the 100% fit, and zero indicates no correlations.

4 Results and Discussion

An overview of the work-flow of applying the C-EnKF technique to calibrate the IRI-2016 model is presented in Fig. (2). The procedure is divided into three levels. In 1- observation level, the IGS stations within Europe are used to estimate STECs and VTECs as described in Section 2.1. The latter is used as observation to tune the parameters of IRI-2016. In 2- model level, the Global Sensitive Analysis (GSA) approach of Section 3.1 is applied to detect key parameters of IRI-2016, which are found to be four, i.e., $URSI(771)$, $URSI(1752)$, $URSI(1327)$, and IG_{12}. Then, these parameters are calibrated through the C-EnKF method as described in Section 3.2. During 3- validation level, we insert the calibrated parameters in Eq. (26) to simulate and forecast ionosphere parameters such as VTEC, Electron density, and $foF2$. These estimates are compared with different observations such as independent GNSS stations, IONEX maps, Radio Occultation (RO) profiles and ionosonde stations will be demonstrated in Sections 4.2 and 4.3.

Before discussing the calibration results, we justify our choice of four calibration parameters. For this, the empirical covariance matrix is computed using the network-derived VTECs and 10 arbitrary parameters that are likely the most sensitive. Our covariance estimation follows the approach in *Schumacher et al.* (2015) during September 2017, where 90 ensemble members are used for computations. The Correlation Coefficients (CCs) between each parameters and the grid point averaged VTECs demonstrate whether these observations will be able to calibrate the parameters. The results are shown in Fig. (3) that correspond to the longitude 15° and different latitudes at the range of 30°N − 75°N. The figure shows that the highest positive and negative CCs (for IG_{12}, $URSI(771)$, $URSI(1327)$ and $URSI(1752)$) are 75%, 47%, -30% and 42%, respectively. These highest values are associated with the four parameters, which are identified by GSA (Section 3.1). This investigation convinces us that the parameters are correctly selected and can be (re-)calibrated by the C-EnKF procedure.

During the calibration procedure, 90 ensemble members of IRI-2016 are generated (Eq. (15)), where the parameters are drawn from Gaussian distribution (shown by $N(\text{mean}, \text{standard deviation})$) as: $\text{URSI}_{1327} \sim N(158.74, 1.58)$, $\text{URSI}_{771} \sim N(128.47, 1.28)$, $\text{URSI}_{1752} \sim N(-142.64, 1.42)$, and $C_{IG} \sim N(0, 10)$ (the bias of IG_{12} is called C_{IG}). Using an empirical iterative approach, we found that using GPS observation (with 15 minutes sampling rate during 24-h) provides the least fitting errors to validate or predict VTECs for the same or next day. Therefore,

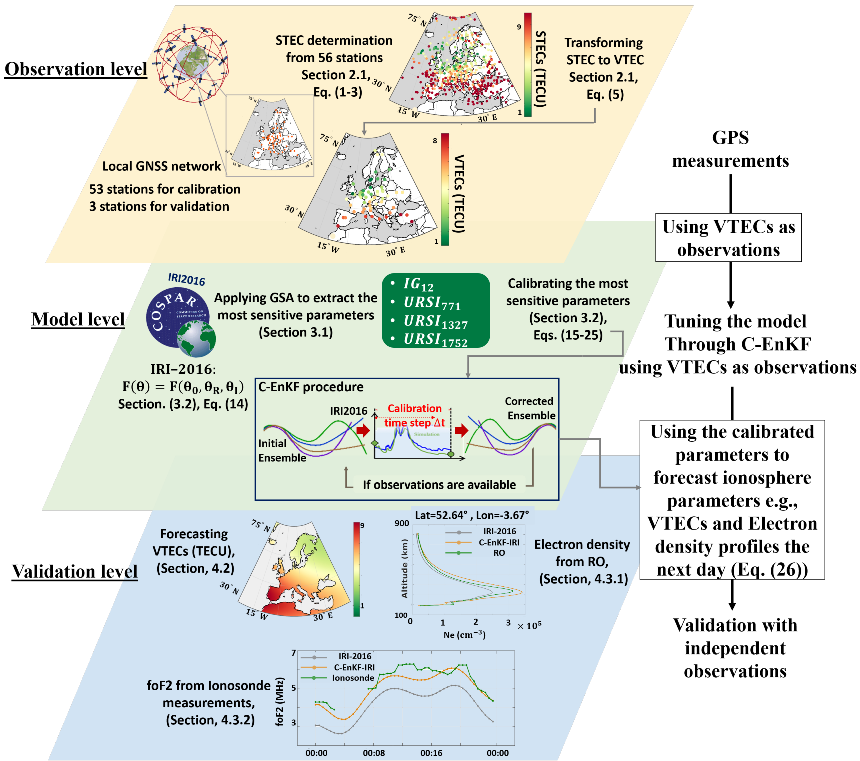

Fig. 2: An overview of the C-EnKF procedure and validation applied on the IRI-2016 to localize it for simulating and forecasting VTECs within Europe. The procedure is divided into three levels: 1- observation (on top), 2- model (middle), and 3- validation levels (bottom).

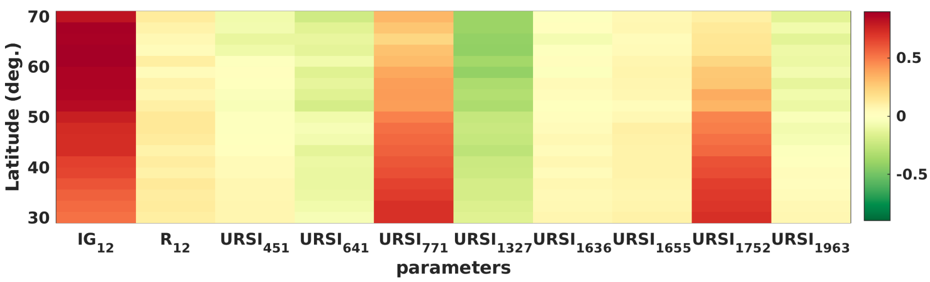

Fig. 3: Averaged Correlation Coefficients (CCs) between 10 model parameters and VTECs obtained from the IRI-2016 model during September 2017. Results correspond to an arbitrary grid points with the longitude of 15°E and the latitudes of 30°N – 75°N.

each day (24 Hours) contains 96 steps, where for each step, a set of calibrated parameters is determined (Eq. (20)). This procedure often converges before 12 hours (i.e., after 12 hours, the calibrated parameters do not considerably change). Eventually, the calibrated parameters replace the default values of IRI-2016. These parameters then can be used to estimate VTECs in the analysis and forecasting steps (e.g., Eqs. (25) and (26)). The new model is abbreviated as 'C-EnKF-IRI'.

In what follows, VTEC estimates of C-EnKF-IRI are assessed in three different ways: in Section 4.1, the VTEC estimates of IRI-2016 and C-EnKF-IRI are compared with those of GNSS-derived VTECs in 56 stations (Fig. (4a)) during the analysis mode to understand how the calibration procedure changed the original IRI-2016 model. In Section 4.2, the forecasting performance of C-EnKF-IRI is validated against the GNSS-derived and IONEX VTECs. In addition, the validation of C-EnKF approach against electron density from COSMIC and $foF2$ from ionosode are presented in Section 4.3. Finally, in Section 4.4, the forecasting performance of C-EnKF-IRI is compared with Klobuchar, NeQuick, IRI-2016 and final product of IONEX models to compute ionospheric delays in SPP application. This is shown for two of validation stations (GRAZ and PTBB) during September 2017.

4.1 Comparison of C-EnKF-IRI with GNSS-derived VTEC Measurements

To evaluate the performance of calibration, the analysis results (Eq. (25)) are assessed by computing the RMSE (Eq. (29)) between models estimates (i.e., IRI-2016 and C-EnKF-IRI) and the network-derived VTEC estimates for 56 stations in Fig. (4) during September 2017 with different geomagnetic (3nT − 106.2nT) and solar activity ($71 - 185sfu$) conditions. The results show that after implementing the C-EnKF, the overall RMSE is reduced by 42.3% (computed in Eq. (30)). Particularly, Fig. (4a) demonstrates the spatial distribution of average improvements at 0h, 4h, 8h, 12h, 16h, and 20h UT for the entire period. The values range between 31% and 60%, and the average values at 12 UT are found to be bigger (on average 54.5%) because the accuracy of IRI-2016 around 12 UT on each day is worse than other times of the day. The daily spatial average of RMSEs during the entire month is shown in Fig. (4b), which indicates 42.3% reduction in RMSE (the range of reduction was between 2.5% and 73.68%). Therefore, these results indicate that the VTEC estimates of C-EnKF-IRI are closer to those from dual frequency GPS measurements during the analysis step. Though this step is not an independent validation, it shows that the selection of parameters in the analysis step was correct and the impact of VTEC observations can correctly be introduced to the model through the calibration procedure.

In Table 1, RMSE (Eq. (29)), AAPD (Eq. (31)), and NRMSE (Eq. (32)) for the validation stations (GRAZ, M0SE, and PTBB), during September 21^{st} and 4^{th}, 2017, with low and high solar activity (i.e., $F_{10.7}$ values of these days were 73 sfu and 183 sfu, respectively) are summarized. The numerical results indicate that the VTECs of C-EnKF-IRI are of higher quality than those of IRI-2016. The monthly average of RMSE in the analysis mode for these stations decreases from 3.2 TECU, 3.9 TECU, and 2.3 TECU to 1.19 TECU, 1.43 TECU, and 0.98 TECU, respectively.

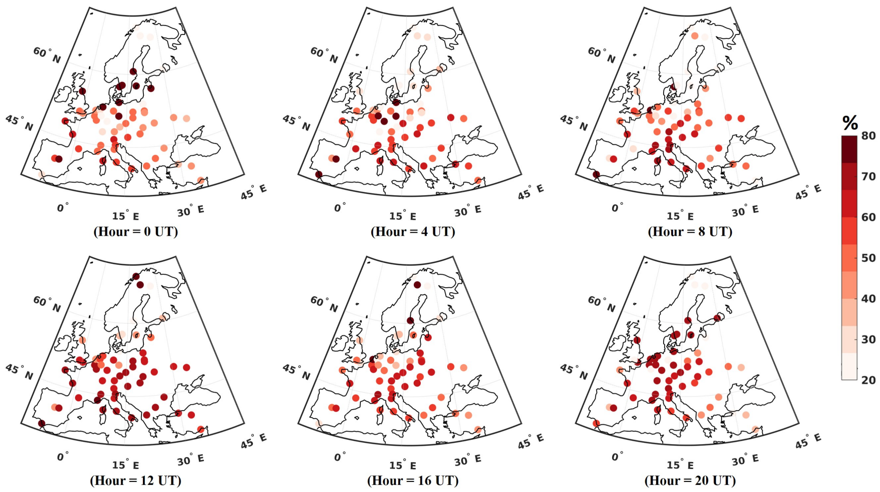

(a) Spatial distribution of the improvements (Eq. (30)) during September 2017 derived in the analysis phase. The presented value for each station is the mean of daily improvements over one month by comparing the VTEC simulations of the original IRI-2016 and C-EnKF-IRI with those derived from the dual frequency GPS measurements.

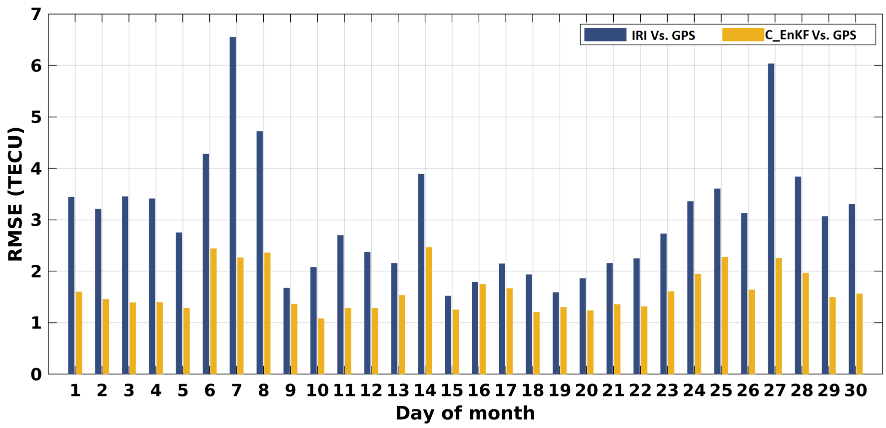

(b) An overview of the daily spatial average of RMSEs that are computed for IGS stations within Europe during September 2017.

Fig. 4: A comparison of spatial and temporal variation of RMSEs between the original IRI-2016 and C-EnKF-IRI compared to the VTEC estimates derived from dual frequency GPS measurements during September 2017.

Table 1: A summary of RMSE, AAPD and NRMSE measures to assess the analysis step of C-EnKF-IRI for 3 validation stations (in Fig. (1)) within Europe. These values correspond to September 21^{st} and 4^{th}, 2017.

(a) The evaluation criteria on September 21^{st}, 2017 (low solar activity)

Stations (Lat [deg] , Long [deg])	RMSE [TECU]		AAPD [%]		NRMSE	
	IRI-2016 Vs. GNSS	C-EnKF-IRI Vs. GNSS	IRI-2016 Vs. GNSS	C-EnKF-IRI Vs. GNSS	IRI-2016 Vs. GNSS	C-EnKF-IRI Vs. GNSS
GARZ (47.07 , 15.49)	2.40	1.00	29.10	10.20	0.22	0.67
M0SE (41.89 , 12.49)	3.35	1.36	33.67	12.69	0.05	0.61
PTBB (52.30 , 10.46)	1.07	0.76	15.45	9.76	0.61	0.72

(b) The evaluation criteria on September 4^{th}, 2017 (high solar activity).

Stations (Lat [deg] , Long [deg])	RMSE [TECU]		AAPD [%]		NRMSE	
	IRI-2016 Vs. GNSS	C-EnKF-IRI Vs. GNSS	IRI-2016 Vs. GNSS	C-EnKF-IRI Vs. GNSS	IRI-2016 Vs. GNSS	C-EnKF-IRI Vs. GNSS
GARZ (47.07 , 15.49)	3.76	0.96	37.32	8.53	-0.14	0.70
M0SE (41.89 , 12.49)	5.26	1.59	43.43	13.38	-0.48	0.54
PTBB (52.30 , 10.46)	2.13	0.92	25.82	12.62	0.29	0.69

A more comprehensive validation under different geomagnetic conditions is achieved by processing the differences between the original IRI-2016 or C-EnKF-IRI and the VTEC estimates from dual frequency GPS measurements during September 2017. The bottom panel of Fig. (5) shows daily Kp (from 2 to 8) and daily mean Disturbance Storm Time (DST, *Gonzalez et al.*, 1999) changing from $-88nT$ to $22nT$. The latter is downloaded from `http://wdc.kugi.kyoto-u.ac.jp/dst_realtime/` and represents the strength and duration of geomagnetic storms for one month. The plots indicate that the selected period covers different levels of geomagnetic activity. In addition, Fig. (5) shows the daily bias (Eq. 27) and RMSE (Eq. 29) results from the original IRI-2016 and C-EnKF-IRI VTECs with the reference to those of the three validation stations. It can be seen that these measures decrease, i.e., the averaged Bias/RMSE reduces from 3.5 TECU/3.8 TECU to 0.73 TECU/1.5 TECU. Thus, we conclude that the C-EnkF-IRI is effective for forecasting VTEC during different geomagnetic activity levels. Particularly, during the storms, the average of improvement for the three validation stations is found to be 72.2%, 64.9%, 70.1% and 58.7% during September 7^{th}, 8^{th}, 27^{th}, and 28^{th}. The considerable improvements after the calibration indicate that the short-term ionospheric dynamics (e.g., calibrating the ionospheric activity index IG_{12}) are better introduced to the model, see Figs. (4b) and (5).

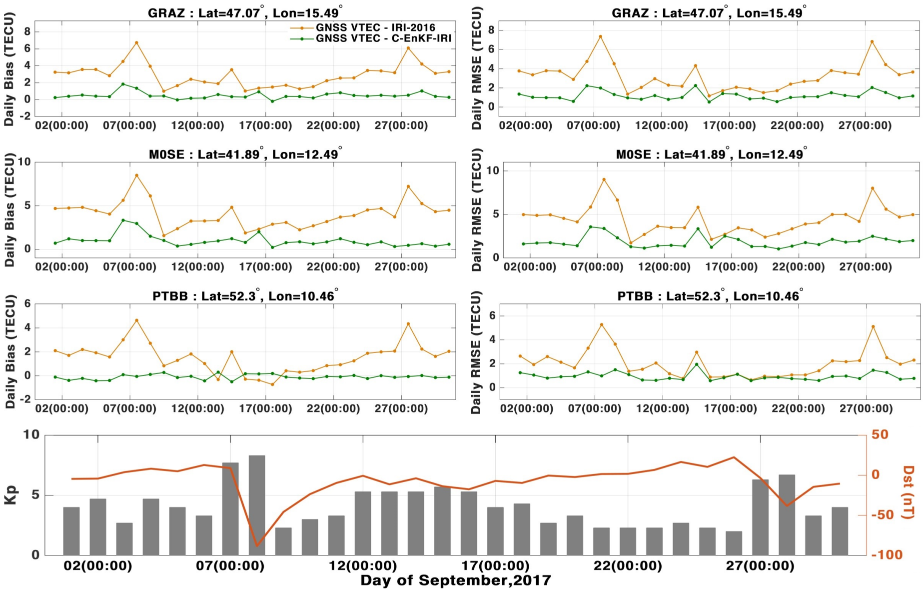

Fig. 5: Daily biases and RMSEs of VTEC estimates derived from the original IRI-2016 and C-EnKF-IRI when they are compared with the VTEC estimates of the validation stations during September 2017 (DOY 244-273).

4.2 Regional Validations of the VTEC Forecasts

In this section, C-EnKF-IRI is assessed in the forecasting phase, for which the set of calibrated parameters in 24 hours are used to forecast VTEC values of the next 24 hours (Eq. 26). These forecasts are performed for 29 days (2^{nd}-30^{th}) of September 2017. On average, over Europe, the mean of RMSE between the original IRI-2016 and the GNSS-derived VTEC estimates was found to be 2.5 TECU, whereas that of C-EnKF-IRI and observations was found to be 1.1 TECU. To illustrate the temporal evolution, Figs. (6a) and (6b) present the VTEC forecasts for some selected stations, where those of the NeQuick, original IRI-2016, C-EnKF-IRI, final product of IONEX and GNSS stations are shown during September 5^{th} and 22^{nd}, with relatively high ($F_{10.7} = 120 sfu$) and low ($F_{10.7} = 85 sfu$) solar activity, respectively. The monthly average of statistical measures are presented in Table 2. These results indicate that not only the RMSE of VTEC estimates and biases are reduced, but also the CCs between the daily forecast of VTECs and observations are increased.

Table 2: A summary of averaged evaluation criteria from the forecasting phase. The values are estimated by comparing the VTECs of the NeQuick, original IRI-2016, C-EnKF-IRI and final product of IONEX with those of IGS stations during September 2017.

Stations (Lat [deg] , Long [deg])	RMSE [TECU]				Bias [TECU]				CC			
	NeQuick Vs. GNSS	IRI-2016 Vs. GNSS	IONEX Vs. GNSS	C-EnKF-IRI Vs. GNSS	NeQuick Vs. GNSS	IRI-2016 Vs. GNSS	IONEX Vs. GNSS	C-EnKF-IRI Vs. GNSS	NeQuick Vs. GNSS	IRI-2016 Vs. GNSS	IONEX Vs. GNSS	C-EnKF-IRI Vs. GNSS
JOZ2 (52.1 , 21.03)	2.66	2.07	0.98	1.4	-1.36	1.62	-0.75	-0.22	0.94	0.94	0.98	0.95
M0SE (41.89 , 12.49)	3.01	4.01	1.2	2.29	0.41	3.65	0.89	0.49	0.93	0.93	0.97	0.96
ORID (41.13 , 20.79)	3.52	4.14	1.25	2.52	-0.32	3.8	0.95	0.51	0.93	0.92	0.97	0.93
PTBB (52.30 , 10.46)	2.57	1.78	1.08	1.41	-1.41	1.31	-1.03	-0.49	0.95	0.95	0.99	0.96
OAK2 (51.12 , -0.91)	2.61	1.95	0.77	1.55	-0.98	1.50	-0.64	-0.43	0.95	0.95	0.99	0.96
YEBE (40.52 , -3.09)	3.53	3.30	1.98	2.76	-1.21	2.18	0.01	-1.33	0.986	0.96	0.98	0.97
GRAZ (47.07 , 15.49)	2.93	2.90	0.72	1.63	-0.81	2.56	-0.17	0.11	0.94	0.94	0.98	0.95

Analogous to Fig. (4a), in Fig. (7), 4-hourly maps of improvements in VTEC estimations are presented in the forecasting phase. This figure shows that the calibrated model is effective in all Europe, though, the magnitude of improvements might be slightly different in different locations and different hours of the day. Overall, C-EnKF-IRI is able to reduce the errors by $\sim 40\%$ during different hours of a day. Different statistical measures such as bias, standard deviation of RMSE values, and the range of improvements are reported in Table 3.

Table 3: Summary of averaged statistical measures derived in the forecasting phase. The values are computed by comparing the VTEC estimates of the original IRI-2016 and C-EnKF-IRI with those of GNSS measurements during September 2017.

Hour (UT)	IRI-2016 Mean of RMSE [TECU]	IRI-2016 Std of RMSE [TECU]	C-EnKF-IRI Mean of RMSE [TECU]	C-EnKF-IRI Std of RMSE [TECU]	Range of improvement [%]
0	2.1591	0.589	1.3621	0.575	[46.95 , 61.48]
4	1.9951	0.346	1.2093	0.228	[33.53 , 56.11]
8	2.6426	0.517	1.8698	0.443	[31.23 , 48.23]
12	3.2873	0.662	1.8899	0.527	[8.46 , 45.50]
16	3.0392	0.628	1.9373	0.495	[23.32 , 60.23]
20	1.9586	0.461	1.4886	0.372	[3.77 , 53.64]

4.3 Validating C-EnKF-IRI with COSMIC Radio Occultation and Ionosonde Data

In this section, we go one step further in validating the C-EnKF-IRI model, and will compare its electron density (Ne) profiles and critical frequency in the F2 ($foF2$) layer instead of focusing on the integrated values of VTEC. For this, Ne profiles and $foF2$ of the original IRI-2016 model and C-EnKF-IRI are compared with the COSMIC radio occultation and in-situ ionosonde data, respectively.

4.3.1 Validation Against COSMIC Data

The COSMIC data are available as 'ionPrf' products (from `http://www.cosmic.ucar.edu`), and their accuracy is generally about 10^4–10^5 cm^{-3} (*COSMIC Program Office*, 2013). Before validating the proposed method with RO data, it is necessary to perform some quality control tests on the individual ionospheric electron density profiles. For this purpose, the least squares method is used to fit a two-layer Chapman function to each profile (*Lei et al.*, 2007). This makes the best fit with RO electron density profiles at the F2 layer. In addition, we estimated the mean deviation of the electron density profiles to quantify the effect of ionospheric plasma irregularities on the height variation in the electron density following *Yang et al.* (2009). In the following, we represent the two COSMIC samples related to an unsuitable (left) and a suitable (right) electron density profile in Fig. (8).

The effect of C-EnKF-IRI in forecasting Ne is shown here as an example during September 5^{th}, 8^{th}, 10^{th} and 13^{th} with different Kp index $Kp = 4$, $Kp = 8$, $Kp = 3$ and $Kp = 5$, respectively (see Fig. (9)). Here, only those data are selected, whose COSMIC tangent point trajectory is entirely within Europe. The results indicate improvements in the range of $33.5\% - 84.6\%$ in the estimations of Ne for the height of $> 300km$. At the bottom of ionosphere (i.e., the height $< 300km$) , the accuracy of the COSMIC data is questionable (*Lei et al.*, 2007; *Yue et al.*, 2011; *Pedatella et al.*, 2015), thus, the corresponding values are ignored in computing the evaluation measures.

To investigate the impact of C-EnKF in simulation Ne during quiet and storm conditions, Relative Differences (RD, Eq. (28)) between the original IRI-2016, as well as C-EnKF-IRI and those of RO are calculated. These values are then used in following Eq. (28) to compute the percentage of improvements as shown in

Fig. (9). The mean improvement of RD in forecasting Ne under quiet and storm conditions is found to be $\sim$ 33% and 39%, respectively.

4.3.2 Validation Against Ionosonde Data

Here, we perform a comparison of the $foF2$ values, which represent the critical frequency in the F2 layer (*McNamara and Thompson*, 2015), provided by five in-situ ionosonde stations (available from `https://www.ukssdc.ac.uk/cgi-bin/digisondes/cost_database.pl`) and those of models. Comparisons are shown in Fig. (10), and the numerical results are reported in Table 4. After implementing C-EnKF, the overall RMSE during September 2017 is reduced by 36%, 39%, 32%, 42%, and 37% in Chilton (longitude: 1.3°W and latitude: 51.6°N, United Kingdom), Dourbes (longitude: 4.6°E and latitude: 50.1°N, Belgium), Juliusruh (longitude: 13.4°E and latitude: 54.6°N, Germany), Moscow (longitude: 37.3°E, latitude: 55.5°N, Russia), and Rome (longitude: 12.5°E and latitude: 41.9°N, Italy), respectively. Therefore, C-EnKF-IRI is expected to be more efficient than the original IRI-2016 in describing ionosphere variables such as the $foF2$ and Ne values.

Table 4: A summary of averaged statistical measures derived by comparing the original IRI-2016 as well as C-EnKF-IRI with the $foF2$ from five ionosonde stations in Europe (Chilton, Dourbes, Juliusruh, Moscow and Rome). Model outputs that are used in the computation correspond to the forecasting phase during September 2017.

Model	RMSE [MHz]		NRMSE		AAPD [%]	
	IRI-2016	C-EnKF-IRI	IRI-2016	C-EnKF-IRI	IRI-2016	C-EnKF-IRI
Chilton	1.226	0.774	-0.063	0.328	21.464	11.662
Dourbes	1.191	0.722	0.048	0.422	20.574	11.159
Juliusruh	1.149	0.780	0.010	0.328	20.597	12.862
Moscow	1.092	0.630	-0.040	0.399	19.095	10.295
Rome	0.974	0.613	0.238	0.520	15.765	9.292

4.4 The Assessment of C-EnKF-IRI in SPP Applications

Two IGS stations (i.e., GRAZ and PTBB in Austria and Germany, respectively, see Fig. (1)) are chosen to evaluate the skill of empirical models in SPP applications. For this, the equivalent ionospheric delays (corresponding to the ionospheric TEC changes) are computed using Eq. (1). VTECs of models are converted to STEC using the inverse of mapping function (Eq. (5)). Then, the corresponding ionospheric delays are determined by Eq. (1). Therefore, in each day, the slant delays between in-situ stations and 32 GPS satellites (when available) are computed. The corresponding estimates (using the same receiver/satellite positions and time steps) are used to estimate delays using empirical models. Here, we compare the performance of the VTEC forecasts of C-EnKF-IRI with those of Klobuchar, the original IRI-2016, and NeQuick models, as well as those of the 2-hourly IONEX fields.

Figures (11a) and (11b) show the RMSEs of delays (in m) that are derived by comparing those of empirical models the direct linear combination of dual frequency GPS measurements, using Eq. (29), on September 21^{st} and 4^{th}, 2017, respectively. These results can be interpreted as slant elevation errors, where those of C-EnKF-IRI and IONEX are found to be the lowest (with the mean and range of 0.33m [0.30m − 0.40m] and 0.34m [0.24m − 0.53m], respectively). Those of Klobuchar, IRI-2016, and NeQuick are found to be considerably bigger, i.e., (with the mean and range of 1.68m [0.64m − 3.90m], 0.73m [0.27m − 4.28m], and 0.72m [0.29m − 1.67m], respectively). Detailed statistical assessments for the entire September 2017 are summarized in Table 5.

Table 5: A summary of RMSE of ionospheric delay estimates derived by comparing the original IRI-2016, C-EnKF-IRI, Klobuchar, NeQuick, and final product of IONEX with those derived from analyzing dual frequency GPS measurements. The evaluations correspond to: 1) September 21^{st}, 2017 (low solar activity $F_{10.7} = 73$ sfu), 2) September 4^{th}, 2017 (high solar activity $F_{10.7} = 183$ sfu), and 3) temporal average of the RMSE estimates during the entire September 2017.

Date	Station	Klobuchar	Nequick	IRI-2016	IONEX	C-EnKF-IRI
Sept. 21^{st}	GRAZ	1.3889 m	0.3851 m	0.5298 m	0.3459 m	0.2986 m
	PTBB	1.5893 m	0.2914 m	0.3536 m	0.2839 m	0.2678 m
Sept. 4^{th}	GRAZ	1.8068 m	1.1841 m	0.8629 m	0.3239 m	0.2979 m
	PTBB	1.9202 m	1.1537 m	0.5929 m	0.2777 m	0.3033 m
entire Sept.	GRAZ	1.6856 m	0.7295 m	0.7210 m	0.3380 m	0.3466 m
	PTBB	1.7639 m	0.6559 m	0.5323 m	0.2805 m	0.3103 m

Assessments of the C-EnKF-IRI VTEC in terms of its impact on positioning accuracy are performed during September 4^{st} and 21^{th}, 2017 with high and low solar activity index, respectively. The processing strategy and the error modelling for the performed SPP experiments are summarized in the following: observations are selected to be pseudo-range measurements from GPS; satellite positions at the transmission epoch computed from their broadcast ephemeris; for troposphere corrections we used the Saastamoinen model (*Saastamoinen*, 1972) and the Global Mapping Function (GMF, *Boehm et al.*, 2006); the elevation cut-off angle and the sampling interval are chosen to be 10 degree and 30 seconds, respectively. To investigate the impact of VTEC modelling on the position accuracy, the SPP experiment is repeated five times with the same setup but for estimating the ionospheric delays, the Klobuchar, NeQuick, IRI-2016, and C-EnKF-IRI model outputs, as well as the IONEX (final) products of IGS center are used. Following these setups, we can obtain five position estimations that are only different in the input used for the reduction of the ionospheric effects.

For numerical assessments, the Root Mean Squares Error (RMSE) (Eq. (29)) between the final solutions of SPP (i.e., the final estimation of station coordinates in the SPP strategy) is calculated. As our reference, the SPP coordinates, whose ionosphere effect was corrected by the final IONEX TEC products are considered as reference. This is chosen following the recommendation of previous studies who found the IONEX TEC to be well suited for the SPP experiments (*Rovira-Garcia et al.*, 2020; *Rovira-Garcia et al.*, 2015; *Liu*, 2016; *Håkansson*, 2020). This means that each SPP coordinates of other four scenarios that are closer to the reference (smaller RMSE) can be considered as the desired approach.

Figure 12 shows the computed position differences on September 4^{st}, 2017. Plots indicate that the use of C-EnKF-IRI for computing the ionospheric corrections reduces the positioning differences with the reference positions, mean of −0.03 m, which is considerably smaller than those SPP solutions corrected by Klobuchar, NeQuick and IRI-2016, where the differences of 1.13m, 2.05m and −0.51m were found, respectively. Table 6 summarizes the numerical results, which shows the final coordinates solution of the SPP corrected by C-EnKF-IRI are very close to the final coordinates of the SPP solution driven by the IONEX TEC. Furthermore, its positioning uncertainties is found smaller than the other experiments (compare the columns 4^{th}, 6^{th}, 8^{th} and 10^{th} of Table 6.

Table 6: A summary of RMSE between final solutions and uncertainties of SPP derived from Klobuchar, NeQuick, original IRI-2016, C-EnKF-IRI compared to the final IONEX product (IGSG). The RMSE between final solutions and uncertainties are called $\mathrm{RMSE_{Sol}}$ and $\mathrm{RMSE_{Unc}}$, respectively. The evaluations correspond to: 1) September 21^{st}, 2017, 2) September 4^{th}, 2017.

Date	Station	Klobuchar		Nequick		IRI-2016		C-EnKF-IRI	
		$\mathrm{RMSE_{Sol}}$ [m]	$\mathrm{RMSE_{Unc}}$ [m]	$\mathrm{RMSE_{Sol}}$ [m]	$\mathrm{RMSE_{Unc}}$ [m]	$\mathrm{RMSE_{Sol}}$ [m]	$\mathrm{RMSE_{Unc}}$ [m]	$\mathrm{RMSE_{Sol}}$ [m]	$\mathrm{RMSE_{Unc}}$ [m]
Sept. 21^{st}	GRAZ	1.98	1.96	0.51	1.69	0.62	1.75	0.08	1.22
	PTBB	1.79	2.84	0.69	1.15	0.81	1.21	0.38	0.97
Sept. 4^{th}	GRAZ	2.43	1.94	4.89	3.87	1.3	2.51	0.13	1.32
	PTBB	2.11	3.59	4.03	5.38	1.32	1.14	0.34	1.41

In comparison with Klobuchar, NeQuick and IRI-2016 models, the use of C-EnKF-IRI model improves the positioning accuracy by 94%, 97% and 89% for GRAZ station, as well as 83%, 91% and 73% for PTBB station during September 4^{th}. These values are found to be 95%, 83% and 86% for GRAZ station, as well as 78%, 44% and 53% for PTBB station during September 21^{st}, respectively. The differences in the magnitude of improvements are related to the differences in solar activity of these two days. Since the use of IONEX TEC fields for SPP applications is recommended (*Su et al.*, 2019b), these results justify that C-EnKF-IRI can be potentially performed in near real-time positioning applications without risking the accuracy.

5 Conclusion

In this study, a sequential Calibration based on the Ensemble Kalman Filter (C-EnKF) is presented, which can be used to localize available ionosphere models in regions of interest using the observations of regional GNSS networks. The numerical assessments of this study are performed based on the IRI-2016 model (*Bilitza*, 2018) and the IGS network in Europe. The daily GNSS-derived VTEC estimates (from 53 IGS stations) are used in the C-EnKF procedure to tune the IRI-2016 model in Europe, so that the new model is called 'C-EnKF-IRI'. Observations of three other IGS stations (GRAZ, MOSE, and PTBB in Austria, Italy and Germany, respectively) are used for validations. The analysis and forecasting skills of the proposed method are assessed in September 2017. Thereafter, comparisons are performed to evaluate the forecasting skills of C-EnKF-IRI in simulating electron density (Ne) of Radio Occultation (RO) and the peak frequency in F2 layer ($foF2$) as observed by ionosonde stations, as well as for estimating the ionospheric delays between in-situ stations and GPS satellites. These results are compared to the mostly used models and products including the original IRI-2016, Klobuchar, NeQuick, and hourly IONEX fields.

The mains findings of this study can be summarized as:

- The C-EnKF is implemented here by considering 90 ensemble members, while integrating 15 minutes of GPS-VTEC estimates into IRI-2016. The new calibrated model (C-EnKF-IRI) provides better VTEC estimates (than the original IRI-2016) especially in days (and at those times of the day) with more pronounced ionospheric dynamics.
- C-EnKF-IRI performs better than the original IRI-2016 in both simulating and forecasting VTECs. Numerical results indicate smaller Root Mean Squares of Error (RMSE) and Average of Absolute Percentage Deviations (AAPD), as well as higher Normalized Root Mean Square Error (NRMSE) and Correlation Coefficients (CCs) with the VTEC estimates from dual frequency GPS measurements compared to the original IRI-2016. The monthly averages of these statistical measures in the analysis step of C-EnKF-IRI in September 2017 are found to be improved, respectively, from the original values of 2.86 (TECU), 33.18%, -0.166, and 80.63% to the calibrated values of 1.58 (TECU), 25.67%, 0.323 and 81.4%, respectively. The C-EnKF-IRI also shows acceptable performance in the forecasting step, where the RMSE (Eq. (29)), AAPD (Eq. (31)), NRMSE (Eq. (32)), and CC (Eq. (33)) measures are found to be on average 1.84 (TECU), 28.42%, 0.187, and 80.93%, while those of the original IRI-2016 are 2.75 (TECU), 32.00%, -0.155, and 77.74%, respectively.
- Comparisons between C-EnKF-IRI and original IRI-2016 against the electron density and $foF2$ from RO and Ionosonde measurements demonstrate the forecasting skills of C-EnKF-IRI in simulating ionosphere properties (i.e., Ne and $foF2$). In terms of Ne, the average of Relative Differences (RD, Eq. (28)) improves 38.1% and higher agreements are found in upper ionosphere (height $> 300km$). In addition, the monthly average of RMSEs decreased up to 37.2% in the 24 hours prediction of $foF2$ and between IRI-2016 and C-EnKF-IRI as shown by the five ionosonde stations within Europe.
- Investigations of C-EnKF-IRI and other empirical models to estimate ionospheric delays in SPP applications indicates that the forecasting skill of C-EnKF-IRI is close to the 11-days delayed IONEX fields. The differences between C-EnKF-IRI and other models (such as IRI-2016, Klobuchar and NeQuick) relative to the ionospheric delays from the dual frequency GPS measurements are found to be considerably big, especially for days with high solar activity,

e.g., on September 4^{th}, 2017, the differences are found to be 0.3239 m, 0.8629 m, 1.8068 m, and 1.1841 m, respectively. Also, the difference between solutions derived from IONEX products and empirical models (i.e., Klobuchar, NeQuick, IRI-2016 and C-EnKF-IRI) are computed to be 2.27 m, 4.46 m, 1.32 m and 0.23 m, respectively. These results essentially represent the effect of the vertical component of ionospheric delay on the accuracy of SPP applications.
- The limitation of this study is that the absence of any priory information for model parameters, which might have an impact on the estimation of model covariance and the updates. Nevertheless, the selected distributions for perturbing the model parameters and generating the 90 ensembles seems to work so that the validation measures confirm our experience.

This work can be extended by estimating VTECs by combining more GNSS constellations from Galileo, GLONASS and BeiDou. Other data sources, e.g., radio occultation and satellite altimetry might also be used to improve the spatial coverage of the VTEC measurements. The C-EnKF model can be controlled by imposing constraints on estimable parameters, which is beneficial to keep the calibrated parameters within physically realistic ranges. Furthermore, the impact of C-EnKF on the PPP application is implemented and tested in the future. Such extensions will be subject to future investigations.

Contributions

Mona Kosary: developing the software, testing the methodology on real data, writing the first draft, and performing the validations. Ehsan Forootan: conceptualising the main idea of the research, supervision, adding discussions and suggestions during the development, and benchmarking the methodology. Saeed Farzaneh: writing the first draft and revisions, contributing in developing the software and performing the validations, and supervision. Maike Schumacher: contributing on conceptual developments, advising, proof reading the drafts, and controlling the computations.

Data availability

The GPS data, final precise GPS satellite orbit and clock products that support the findings of this study are available in the Crustal Dynamics Data Information System which can be accessed from ftp://cddis.gsfc.nasa.gov/. The Differential Code Bias (DCB) product are available from http://ftp.aiub.unibe.ch/BSWUSER52/ORB/. The COSMIC data are available from http://www.cosmic.ucar.edu. The Ionosonde data in Eroupe are available from https://www.ukssdc.ac.uk/cgi-bin/digisondes/cost_database.pl. The localized TEC estimates within Europe for the entire September 2017 will be provided by efo@plan.aau.dk per request.

References

Ahluwalia, H. S. (2000), Ap time variations and interplanetary magnetic field intensity, *Journal of Geophysical Research: Space Physics*, *105*(A12), 27,481–27,487, doi:https://doi.org/10.1029/2000JA900124.

Allen, J. (2004), The ap* index of maximum 24-hour disturbance for storm events.

An, X., X. Meng, H. Chen, W. Jiang, R. Xi, and Q. Chen (2020), Modelling global ionosphere based on multi-frequency, multi-constellation GNSS observations and IRI model, *Remote Sensing*, *12*(3), 439, doi:https://doi.org/10.3390/rs12030439.

Andersen, O. B., P. Knudsen, and P. A. Berry (2010), The DNSC08GRA global marine gravity field from double retracked satellite altimetry, *Journal of Geodesy*, *84*(3), 191–199, doi:https://doi.org/10.1007/s00190-009-0355-9.

Aragon-Angel, A., M. Zürn, and A. Rovira-Garcia (2019), Galileo ionospheric correction algorithm: An optimization study of NeQuick-G, *Radio Science*, *54*(11), 1156–1169, doi:https://doi.org/10.1029/2019RS006875.

Bilitza, D. (2001), International reference ionosphere 2000, *Radio Science*, *36*(2), 261–275, doi:https://doi.org/10.1029/2000RS002432.

Bilitza, D. (2018), IRI the international standard for the ionosphere., *Advances in Radio Science*, *16*, doi:https://doi.org/10.5194/ars-16-1-2018.

Bilitza, D., D. Altadill, V. Truhlik, V. Shubin, I. Galkin, B. Reinisch, and X. Huang (2017), International reference ionosphere 2016: From ionospheric climate to real-time weather predictions, *Space Weather*, *15*(2), 418–429, doi:https://doi.org/10.1002/2016SW001593.

Boehm, J., A. Niell, P. Tregoning, and H. Schuh (2006), Global mapping function (GMF): A new empirical mapping function based on numerical weather model data, *Geophysical Research Letters*, *33*(7), doi:https://doi.org/10.1029/2005GL025546.

Borries, C., N. Jakowski, C. Jacobi, P. Hoffmann, and A. Pogoreltsev (2007), Spectral analysis of planetary waves seen in ionospheric total electron content (TEC): first results using GPS differential TEC and stratospheric reanalyses, *Journal of atmospheric and solar-terrestrial physics*, *69*(17-18), 2442–2451, doi:https://doi.org/10.1016/j.jastp.2007.02.004.

Boulic, R., N. M. Thalmann, and D. Thalmann (1990), A global human walking model with real-time kinematic personification, *The visual computer*, *6*(6), 344–358, doi:https://doi.org/10.1007/BF01901021.

Bouya, Z., M. Terkildsen, and D. Neudegg (2010), Regional GPS-based ionospheric TEC model over australia using spherical cap harmonic analysis, *cosp*, *38*, 4.

Brown, S., D. Bilitza, and E. Yigit (2018a), Ionosonde-based indices for improved representation of solar cycle variation in the international reference ionosphere model, *Journal of Atmospheric and Solar-Terrestrial Physics*, *171*, 137–146, doi:https://doi.org/10.1016/j.jastp.2017.08.022, vertical Coupling in the Atmosphere-Ionosphere System: Recent Progress.

Brown, S., D. Bilitza, and E. Yiğit (2018b), Ionosonde-based indices for improved representation of solar cycle variation in the international reference ionosphere model, *Journal of Atmospheric and Solar-Terrestrial Physics*, *171*, 137–146, doi:https://doi.org/10.1016/j.jastp.2017.08.022.

Bust, G., and S. Datta-Barua (2014), Scientific investigations using IDA4D and EMPIRE, *Modeling the Ionosphere-Thermosphere System*, pp. 283–297, doi:

https://doi.org/10.1002/9781118704417.ch23.
Bust, G., T. Garner, and T. Gaussiran (2004), Ionospheric data assimilation three-dimensional (IDA3D): A global, multisensor, electron density specification algorithm, *Journal of Geophysical Research: Space Physics*, *109*(A11), doi: https://doi.org/10.1029/2003JA010234.
CCIR, C. (1967), Atlas of ionospheric characteristics.
COSMIC Program Office (2013), http://cdaac-www.cosmic.ucar.edu/cdaac/products.html.
Daniell, R. E., L. Brown, D. Anderson, M. Fox, P. H. Doherty, D. Decker, J. J. Sojka, and R. W. Schunk (1995), Parameterized ionospheric model: A global ionospheric parameterization based on first principles models, *Radio Science*, *30*(5), 1499–1510, doi:https://doi.org/10.1029/95RS01826.
Dubey, S., R. Wahi, and A. Gwal (2006), Ionospheric effects on GPS positioning, *Advances in Space Research*, *38*(11), 2478–2484, doi:https://doi.org/10.1016/j.asr.2005.07.030.
Engfeldt, A. (2005), *Network RTK in northern and central Europe*, Lantmäteriet.
Erdogan, E., M. Schmidt, A. Goss, B. Görres, and F. Seitz (2020), Adaptive modeling of the global ionosphere vertical total electron content, *Remote Sensing*, *12*(11), 1822, doi:https://doi.org/10.3390/rs12111822.
Evensen, G. (2003), The ensemble Kalman filter: theoretical formulation and practical implementation, *Ocean dynamics*, *53*(4), 343–367, doi:https://doi.org/10.1007/s10236-003-0036-9.
Evensen, G. (2009), The Ensemble Kalman filter for combined state and parameter estimation, *IEEE Control Systems Magazine*, *29*(3), 83–104, doi:https://doi.org/10.1109/MCS.2009.932223.
Farzaneh, S., and E. Forootan (2018), Reconstructing regional ionospheric electron density: a combined spherical slepian function and empirical orthogonal function approach, *Surveys in Geophysics*, *39*(2), 289–309, doi:https://doi.org/10.1007/s10712-017-9446-y.
Farzaneh, S., and E. Forootan (2020), A least squares solution to regionalize VTEC estimates for positioning applications, *Remote Sensing*, *12*(21), 3545, doi:https://doi.org/10.3390/rs12213545.
Feltens, J., and S. Schaer (1998), IGS products for the ionosphere, in *Proceedings of the 1998 IGS Analysis Center Workshop Darmstadt, Germany*, pp. 3–5.
Forootan, E., S. Farzaneh, M. Kosary, M. Schmidt, and M. Schumacher (2020), A simultaneous calibration and data assimilation (C/DA) to improve nrlmsise00 using thermospheric neutral density (TND) from space-borne accelerometer measurements, *Geophysical Journal International*, *224*(2), 1096–1115, doi: 10.1093/gji/ggaa507.
Gan, Y., Q. Duan, W. Gong, C. Tong, Y. Sun, W. Chu, A. Ye, C. Miao, and Z. Di (2014), A comprehensive evaluation of various sensitivity analysis methods: A case study with a hydrological model, *Environmental Modelling and Software*, *51*, 269–285, doi:https://doi.org/10.1016/j.envsoft.2013.09.031.
Goncharenko, L., J. Chau, P. Condor, A. Coster, and L. Benkevitch (2013), Ionospheric effects of sudden stratospheric warming during moderate-to-high solar activity: Case study of january 2013, *Geophysical Research Letters*, *40*(19), 4982–4986, doi:https://doi.org/10.1002/grl.50980.
Gonzalez, W. D., B. T. Tsurutani, and A. L. C. De Gonzalez (1999), Interplanetary origin of geomagnetic storms, *Space Science Reviews*, *88*(3), 529–562, doi:https:

//doi.org/10.1023/A:1005160129098.

Goss, A., M. Schmidt, E. Erdogan, and F. Seitz (2020), Global and regional high-resolution VTEC modelling using a two-step B-spline approach, *Remote Sensing*, *12*(7), 1198, doi:https://doi.org/10.3390/rs12071198.

Groves, P. D. (2015), Principles of GNSS, inertial, and multisensor integrated navigation systems, 2nd edition [book review], *IEEE Aerospace and Electronic Systems Magazine*, *30*(2), 26–27, doi:10.1109/MAES.2014.14110.

He, J., X. Yue, H. Le, Z. Ren, and W. Wan (2020), Evaluation on the quasi-realistic ionospheric prediction using an ensemble Kalman filter data assimilation algorithm, *Space Weather*, *18*(3), e2019SW002,410, doi:https://doi.org/10.1029/2019SW002410.

Hernández-Pajares, M., J. Juan, J. Sanz, R. Orus, A. Garcia-Rigo, J. Feltens, A. Komjathy, S. Schaer, and A. Krankowski (2009), The IGS VTEC maps: a reliable source of ionospheric information since 1998, *Journal of Geodesy*, *83*(3-4), 263–275, doi:https://doi.org/10.1007/s00190-008-0266-1.

Hoque, M. M., N. Jakowski, and J. A. Cahuasquí (2020), Fast ionospheric correction algorithm for Galileo single frequency users, in *2020 European Navigation Conference (ENC)*, pp. 1–10, doi:https://doi.org/10.23919/ENC48637.2020.9317502.

Håkansson, M. (2020), Nadir-dependent GNSS code biases and their effect on 2D and 3D ionosphere modeling, *Remote Sensing*, *12*(6), doi:https://doi.org/10.3390/rs12060995.

ICD (2017a), *BeiDou navigation satellite system signal in space interface control document open service signal B1C (Version 1.0)*, China Satellite Navigation Office, doi:http://www.beidou.gov.cn/xt/gfxz/201712/P020171226741342013031.pdf.

ICD (2017b), *BeiDou navigation satellite system signal in space interface control document open service signal B2a (Version 1.0)*, China Satellite Navigation Office, doi:http://www.beidou.gov.cn/xt/gfxz/201712/P020171226742357364174.pdf.

ICD (2020), *BeiDou navigation satellite system signal in space interface control document open service signal B2b (Version 1.0)*, China Satellite Navigation Office, doi:http://en.beidou.gov.cn/SYSTEMS/ICD/202008/P020200803539206360377.pdf.

Jakowski, N., C. Mayer, M. Hoque, and V. Wilken (2011), Total electron content models and their use in ionosphere monitoring, *Radio Science*, *46*(06), 1–11, doi:https://doi.org/10.1029/2010RS004620.

Jee, G., H.-B. Lee, Y. H. Kim, J.-K. Chung, and J. Cho (2010), Assessment of GPS global ionosphere maps (GIM) by comparison between CODE GIM and TOPEX/Jason TEC data: ionospheric perspective, *Journal of Geophysical Research: Space Physics*, *115*(A10), doi:https://doi.org/10.1029/2010JA015432.

Johnston, G., A. Riddell, and G. Hausler (2017), *The International GNSS Service*, pp. 967–982, Springer International Publishing, Cham, doi:10.1007/978-3-319-42928-1_33.

Jones, W. B., and R. M. Gallet (1962), Representation of diurnal and geographic variations of ionospheric data by numerical methods, *Telecomm. J*, *29*(5), 129–147.

Katamzi, Z., N. Smith, C. Mitchell, P. Spalla, and M. Materassi (2012), Statistical analysis of travelling ionospheric disturbances using TEC observations from

geostationary satellites, *Journal of Atmospheric and Solar-Terrestrial Physics*, *74*, 64–80, doi:https://doi.org/10.1016/j.jastp.2011.10.006.
Kedar, S., G. A. Hajj, B. D. Wilson, and M. B. Heflin (2003), The effect of the second order GPS ionospheric correction on receiver positions, *Geophysical Research Letters*, *30*(16), doi:https://doi.org/10.1029/2003GL017639.
Kelley, M. C. (2009), *The earth's ionosphere: plasma physics and electrodynamics*, Academic press.
Klobuchar, J. A. (1987), Ionospheric time-delay algorithm for single frequency GPS users, *IEEE Transactions on Aerospace and Electronic Systems*, *AES-23*(3), 325–331, doi:https://doi.org/10.1109/TAES.1987.310829.
Krypiak-Gregorczyk, A., P. Wielgosz, and W. Jarmołowski (2017), A new TEC interpolation method based on the least squares collocation for high accuracy regional ionospheric maps, *Measurement Science and Technology*, *28*(4), 045,801, doi:https://doi.org/10.1088/1361-6501/aa58ae.
Kursinski, E. R., G. A. Hajj, J. T. Schofield, R. P. Linfield, and K. R. Hardy (1997), Observing earth's atmosphere with radio occultation measurements using the global positioning system, *Journal of Geophysical Research: Atmospheres*, *102*(D19), 23,429–23,465, doi:https://doi.org/10.1029/97JD01569.
Lei, J., S. Syndergaard, A. G. Burns, S. C. Solomon, W. Wang, Z. Zeng, R. G. Roble, Q. Wu, Y.-H. Kuo, J. M. Holt, et al. (2007), Comparison of COSMIC ionospheric measurements with ground-based observations and model predictions: preliminary results, *Journal of Geophysical Research: Space Physics*, *112*(A7), doi:https://doi.org/10.1029/2006JA012240.
Li, X., and D. Guo (2010), Modeling and prediction of ionospheric total electron content by time series analysis, in *2010 2nd International Conference on Advanced Computer Control*, vol. 2, pp. 375–379, IEEE, doi:https://doi.org/10.1109/ICACC.2010.5486653.
Li, Z., Y. Yuan, N. Wang, M. Hernandez-Pajares, and X. Huo (2015), SHPTS: towards a new method for generating precise global ionospheric TEC map based on spherical harmonic and generalized trigonometric series functions, *Journal of Geodesy*, *89*(4), 331–345, doi:https://doi.org/10.1007/s00190-014-0778-9.
Liou, Y.-A., A. G. Pavelyev, S.-F. Liu, A. A. Pavelyev, N. Yen, C.-Y. Huang, and C.-J. Fong (2007), FORMOSAT-3/COSMIC GPS radio occultation mission: preliminary results, *IEEE Transactions on Geoscience and Remote Sensing*, *45*(11), 3813–3826, doi:https://doi.org/10.1109/TGRS.2007.903365.
Liu, L., Y. Yao, S. Zou, J. Kong, L. Shan, C. Zhai, C. Zhao, and Y. Wang (2019), Ingestion of GIM-derived TEC data for updating IRI-2016 driven by effective IG indices over the European region, *Journal of Geodesy*, *93*(10), 1911–1930, doi:https://doi.org/10.1007/s00190-019-01291-5.
Liu, R. Y., P. A. Smith, and J. W. King (1983), A new solar index which leads to improved foF2 predictions using the CCIR atlas., *Telecommun. J*, *50*(8), 408–414.
Liu, W. (2016), Positioning performance of single-frequency GNSS receiver using Australian regional ionospheric corrections, Master's thesis, Queensland University of Technology.
McNamara, L. F., and D. C. Thompson (2015), Validation of COSMIC values of foF2 and M(3000)F2 using ground-based ionosondes, *Advances in Space Research*, *55*(1), 163–169, doi:https://doi.org/10.1016/j.asr.2014.07.015.

Mengist, C. K., N. Ssessanga, S.-H. Jeong, J.-H. Kim, Y. H. Kim, and Y.-S. Kwak (2019), Assimilation of multiple data types to a regional ionosphere model with a 3D-Var algorithm (IDA4D), *Space Weather*, *17*(7), 1018–1039, doi:https://doi.org/10.1029/2019SW002159.

Mukhtarov, P., B. Andonov, and D. Pancheva (2013), Global empirical model of TEC response to geomagnetic activity, *Journal of Geophysical Research: Space Physics*, *118*(10), 6666–6685, doi:https://doi.org/10.1002/jgra.50576.

Mulassano, P., F. Dovis, and F. Collomb (2004), European projects for innovative GNSS-related applications, *GPS Solutions*, *7*(4), 268–270, doi:https://doi.org/10.1007/s10291-003-0071-5.

Nava, B., P. Coisson, and S. Radicella (2008), A new version of the NeQuick ionosphere electron density model, *Journal of Atmospheric and Solar-Terrestrial Physics*, *70*(15), 1856–1862, doi:https://doi.org/10.1016/j.jastp.2008.01.015.

Nohutcu, M., M. Karslioglu, and M. Schmidt (2010), B-spline modeling of VTEC over Turkey using GPS observations, *Journal of Atmospheric and Solar-Terrestrial Physics*, *72*(7-8), 617–624, doi:https://doi.org/10.1016/j.jastp.2010.02.022.

Nossent, J., P. Elsen, and W. Bauwens (2011), Sobol' sensitivity analysis of a complex environmental model, *Environmental Modelling and Software*, *26*(12), 1515–1525, doi:https://doi.org/10.1016/j.envsoft.2011.08.010.

Øvstedal, O. (2002), Absolute positioning with single-frequency GPS receivers, *GPS Solutions*, *5*(4), 33–44, doi:https://doi.org/10.1007/PL00012910.

Pedatella, N., X. Yue, and W. Schreiner (2015), Comparison between GPS radio occultation electron densities and in situ satellite observations, *Radio Science*, *50*(6), 518–525, doi:https://doi.org/10.1002/2015RS005677.

Pignalberi, A. (2019), A three-dimensional regional assimilative model of the ionospheric electron density, Ph.D. thesis, alma.

Rawer, K., D. Bilitza, and S. Ramakrishnan (1978), Goals and status of the International Reference Ionosphere, *Reviews of Geophysics*, *16*(2), 177–181, doi:https://doi.org/10.1029/RG016i002p00177.

Reinisch, B. W., X. Huang, I. Galkin, and D. Bilitza (2013), Real time assimilative foF2 maps for IRI, in *2013 US National Committee of URSI National Radio Science Meeting (USNC-URSI NRSM)*, pp. 1–1, IEEE.

Rishbeth, H. (1998), How the thermospheric circulation affects the ionospheric F2-layer, *Journal of Atmospheric and Solar-Terrestrial Physics*, *60*(14), 1385–1402, doi:https://doi.org/10.1016/S1364-6826(98)00062-5.

Rose, J. A., R. J. Watson, D. J. Allain, and C. N. Mitchell (2014), Ionospheric corrections for GPS time transfer, *Radio Science*, *49*(3), 196–206, doi:https://doi.org/10.1002/2013RS005212.

Rovira-Garcia, A., J. M. Juan, J. Sanz, and G. González-Casado (2015), A worldwide ionospheric model for fast precise point positioning, *IEEE Transactions on Geoscience and Remote Sensing*, *53*(8), 4596–4604, doi:https://doi.org/10.1109/TGRS.2015.2402598.

Rovira-Garcia, A., D. Ibanez-Segura, R. Orus-Perez, J. M. Juan, J. Sanz, and G. Gonzalez-Casado (2020), Assessing the quality of ionospheric models through GNSS positioning error: methodology and results, *Gps solutions*, *24*(1), 1–12, doi:https://doi.org/10.1007/s10291-019-0918-z.

Saastamoinen, J. (1972), *Atmospheric correction for the troposphere and stratosphere in radio ranging satellites*, pp. 247–251, American Geophysical Union

(AGU), doi:https://doi.org/10.1029/GM015p0247.

Saltelli, A. (2002a), Making best use of model evaluations to compute sensitivity indices, *Computer Physics Communications*, *145*(2), 280–297, doi:https://doi.org/10.1016/S0010-4655(02)00280-1.

Saltelli, A. (2002b), Sensitivity analysis for importance assessment, *Risk analysis*, *22*(3), 579–590, doi:https://doi.org/10.1111/0272-4332.00040.

Saltelli, A., P. Annoni, I. Azzini, F. Campolongo, M. Ratto, and S. Tarantola (2010), Variance based sensitivity analysis of model output. design and estimator for the total sensitivity index, *Computer Physics Communications*, *181*(2), 259–270, doi:https://doi.org/10.1016/j.cpc.2009.09.018.

Sanz Subirana, J., J. Juan Zornoza, and M. Hernández-Pajares (2013), GNSS data processing book, vol. i: fundamentals and algorithms, *Tech. rep.*, TM-23/1. Noordwijk: ESA Communications.

Schaer, S., and S. helvétique des sciences naturelles. Commission géodésique (1999), *Mapping and predicting the Earth's ionosphere using the Global Positioning System*, vol. 59, Institut für Geodäsie und Photogrammetrie, Eidg. Technische Hochschule ....

Schaer, S., G. Beutler, L. Mervart, M. Rothacher, and U. Wild (1996a), Global and regional ionosphere models using the GPS double difference phase observable, in *Proceedings of the IGS Workshop" Special Topics and New Directions"*.

Schaer, S., G. Beutler, M. Rothacher, and T. A. Springer (1996b), Daily global ionosphere maps based on GPS carrier phase data routinely produced by the CODE analysis center, in *Proceedings of the IGS Analysis Center Workshop 1996*.

Scherliess, L., R. W. Schunk, J. J. Sojka, and D. C. Thompson (2004), Development of a physics-based reduced state Kalman filter for the ionosphere, *Radio Science*, *39*(1), 1–12, doi:https://doi.org/10.1029/2002RS002797.

Schumacher, M. (2016), Methods for assimilating remotely-sensed water storage changes into hydrological models, Ph.D. thesis, Rheinische Friedrich-Wilhelms-Universität Bonn.

Schumacher, M., A. Eicker, J. Kusche, H. M. Schmied, and P. Döll (2015), Covariance analysis and sensitivity studies for GRACE assimilation into WGHM, in *IAG 150 Years*, pp. 241–247, Springer, doi:https://doi.org/10.1007/1345_2015_119.

Schunk, R. W., L. Scherliess, J. J. Sojka, D. C. Thompson, D. N. Anderson, M. Codrescu, C. Minter, T. J. Fuller-Rowell, R. A. Heelis, M. Hairston, et al. (2004), Global assimilation of ionospheric measurements (GAIM), *Radio Science*, *39*(1), doi:https://doi.org/10.1029/2002RS002794.

Sobol, I. (2001), Global sensitivity indices for nonlinear mathematical models and their monte carlo estimates, *Mathematics and Computers in Simulation*, *55*(1), 271–280, doi:https://doi.org/10.1016/S0378-4754(00)00270-6, the Second IMACS Seminar on Monte Carlo Methods.

Sobol, I. M. (1990), On sensitivity estimation for nonlinear mathematical models, *Matematicheskoe modelirovanie*, *2*(1), 112–118.

Spalla, P., and L. Cairolo (1994), TEC and foF2 comparison, *Annals of Geophysics*, *37*(5), doi:https://doi.org/10.4401/ag-4182.

Su, K., S. Jin, and M. Hoque (2019a), Evaluation of ionospheric delay effects on multi-GNSS positioning performance, *Remote Sensing*, *11*(2), 171, doi:https://doi.org/10.3390/rs11020171.

Su, K., S. Jin, and M. M. Hoque (2019b), Evaluation of ionospheric delay effects on multi-GNSS positioning performance, *Remote Sensing*, *11*(2), doi:https://doi.org/10.3390/rs11020171.

Tapping, K. F. (2013), The 10.7cm solar radio flux (F10.7), *Space Weather*, *11*(7), 394–406, doi:https://doi.org/10.1002/swe.20064.

Union-Radiocommunication, I. T. (2009), *ITU-R reference ionospheric characteristics*, International Telecommunication Union Geneva.

Verhagen, S., D. Odijk, P. Teunissen, and L. Huisman (2010), Performance improvement with low-cost multi-GNSS receivers, in *Proceedings of the 2010 5th ESA Workshop on Satellite Navigation Technologies and European Workshop on GNSS Signals and Signal Processing (NAVITEC), Noordwijk, The Netherlands, 8–10 December 2010*, pp. 1–8.

Wan, W., F. Ding, Z. Ren, M. Zhang, L. Liu, and B. Ning (2012), Modeling the global ionospheric total electron content with empirical orthogonal function analysis, *Science China Technological Sciences*, *55*(5), 1161–1168, doi:https://doi.org/10.1007/s11431-012-4823-8.

Webb, D. F., and R. A. Howard (1994), The solar cycle variation of coronal mass ejections and the solar wind mass flux, *Journal of Geophysical Research: Space Physics*, *99*(A3), 4201–4220, doi:https://doi.org/10.1029/93JA02742.

Wu, M., P. Guo, T. Xu, N. Fu, X. Xu, H. Jin, and X. Hu (2015), Data assimilation of plasmasphere and upper ionosphere using COSMIC/GPS slant TEC measurements, *Radio Science*, *50*(11), 1131–1140, doi:https://doi.org/10.1002/2015RS005732.

Wu, X., X. Hu, G. Wang, H. Zhong, and C. Tang (2013), Evaluation of COMPASS ionospheric model in GNSS positioning, *Advances in Space Research*, *51*(6), 959–968, doi:https://doi.org/10.1016/j.asr.2012.09.039.

Wübbena, G., M. Schmitz, and A. Bagge (2005), PPP-RTK: precise point positioning using state-space representation in RTK networks, in *Proceedings of ION GNSS*, vol. 5, pp. 13–16.

Yang, K.-F., Y.-H. Chu, C.-L. Su, H.-T. Ko, and C.-Y. Wang (2009), An examination of FORMOSAT-3/COSMIC ionospheric electron density profile: data quality criteria and comparisons with the IRI model, *Terrestrial, Atmospheric and Oceanic Sciences*, *20*(1), 193, doi:http://dx.doi.org/10.3319/TAO.2007.10.05.01(F3C).

Yuan, Y., and J. Ou (2001a), Auto-covariance estimation of variable samples (ACEVS) and its application for monitoring random ionospheric disturbances using GPS, *Journal of Geodesy*, *75*, 438–447, doi:https://doi.org/10.1007/s001900100197.

Yuan, Y., and J. Ou (2001b), An improvement to ionospheric delay correction for single-frequency GPS users–the APR-I scheme, *Journal of Geodesy*, *75*(5-6), 331–336, doi:https://doi.org/10.1007/s001900100182.

Yuan, Y., X. Huo, J. Ou, K. Zhang, Y. Chai, D. Wen, and R. Grenfell (2008a), Refining the klobuchar ionospheric coefficients based on GPS observations, *IEEE Transactions on Aerospace and Electronic Systems*, *44*(4), 1498–1510, doi:https://doi.org/10.1109/TAES.2008.4667725.

Yuan, Y., C. Tscherning, P. Knudsen, G. Xu, and J. Ou (2008b), The ionospheric eclipse factor method (IEFM) and its application to determining the ionospheric delay for GPS, *Journal of Geodesy*, *82*(1), 1–8, doi:https://doi.org/10.1007/s00190-007-0152-2.

Yuan, Y., N. Wang, Z. Li, and X. Huo (2019), The BeiDou global broadcast ionospheric delay correction model (BDGIM) and its preliminary performance evaluation results, *NAVIGATION*, *66*(1), 55–69, doi:https://doi.org/10.1002/navi.292.

Yue, X., W. S. Schreiner, C. Rocken, and Y.-H. Kuo (2011), Evaluation of the orbit altitude electron density estimation and its effect on the abel inversion from radio occultation measurements, *Radio Science*, *46*(1), doi:https://doi.org/10.1029/2010RS004514.

Zhang, B., P. J. Teunissen, Y. Yuan, X. Zhang, and M. Li (2019), A modified carrier-to-code leveling method for retrieving ionospheric observables and detecting short-term temporal variability of receiver differential code biases, *Journal of Geodesy*, *93*(1), 19–28, doi:https://doi.org/10.1007/s00190-018-1135-1.

Zhang, C., J. Chu, and G. Fu (2013), Sobol's sensitivity analysis for a distributed hydrological model of yichun river basin, china, *Journal of Hydrology*, *480*, 58–68, doi:https://doi.org/10.1016/j.jhydrol.2012.12.005.

Zhang, J., J. Gao, B. Yu, C. Sheng, and X. Gan (2020), Research on remote GPS common-view precise time transfer based on different ionosphere disturbances, *Sensors*, *20*(8), 2290, doi:https://doi.org/10.3390/s20082290.

Zumberge, J., M. Heflin, D. Jefferson, M. Watkins, and F. H. Webb (1997), Precise point positioning for the efficient and robust analysis of GPS data from large networks, *Journal of geophysical research: solid earth*, *102*(B3), 5005–5017, doi:https://doi.org/10.1029/96JB03860.

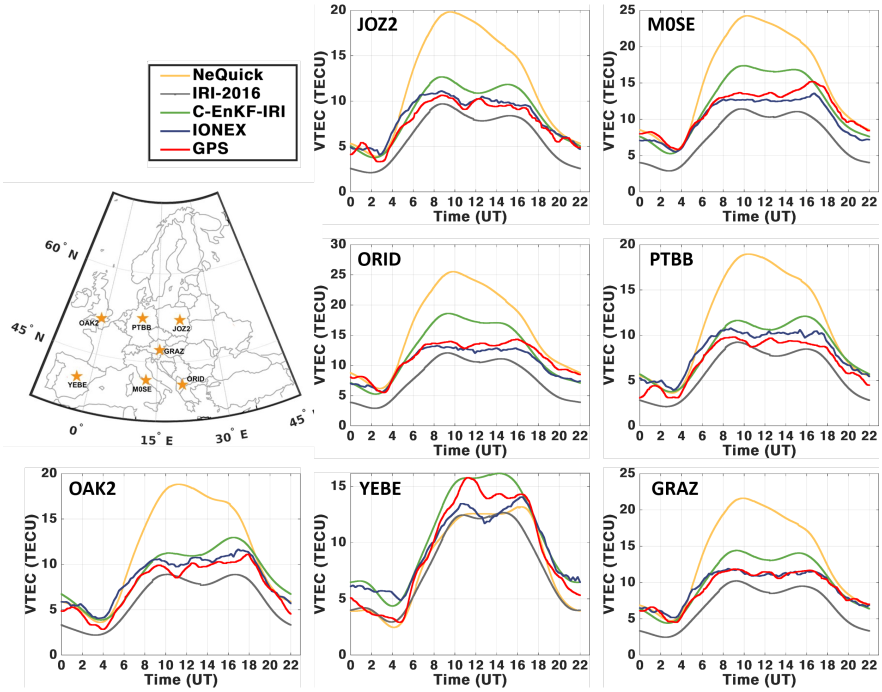

(a) Temporal variation of VTEC estimates during 24 hour on September 5^{th}, 2017.

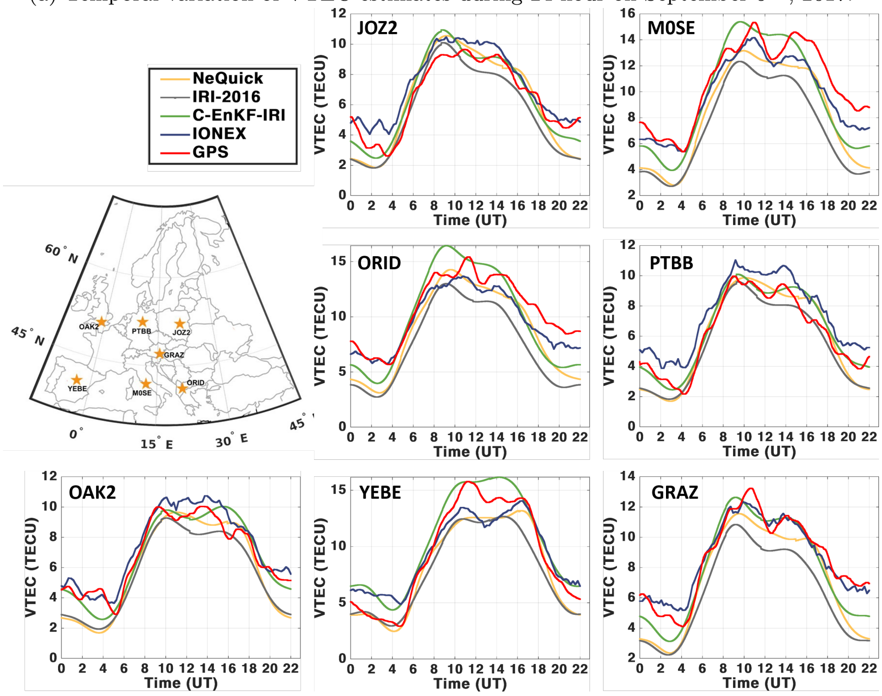

(b) Temporal variation of VTEC estimates during 24 hour on September 22^{nd}, 2017.

Fig. 6: A comparison of temporal variations of VTEC estimates from the NeQuick, original IRI-2016, C-EnKF-IRI, final product of IONEX and those derived from dual frequency GNSS measurements. The VTECs of C-EnKF-IRI are computed in the forecasting phase, i.e., the calibrated parameters of previous day (here on September 4^{th} and 21^{st}, 2017) are used to forecast the VTEC values of the next day (here on September 5^{th} and 22^{nd}, 2017).

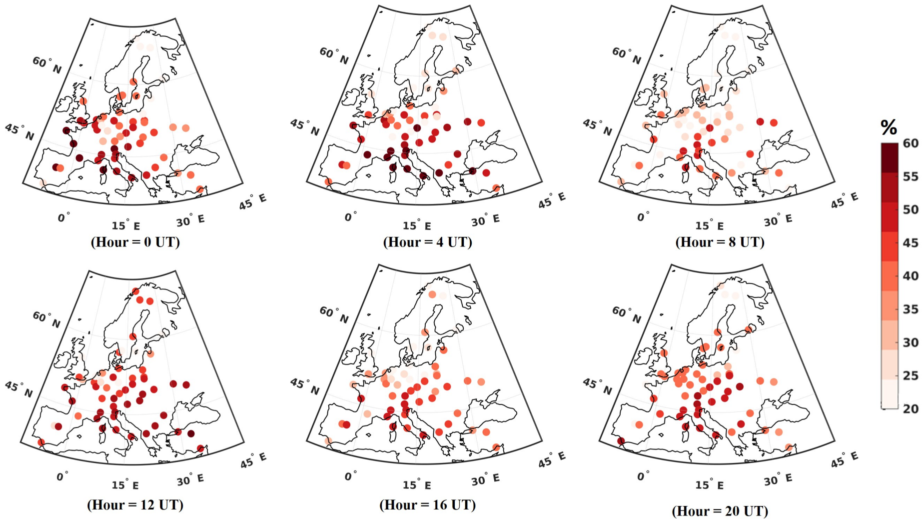

Fig. 7: Spatial distribution of improvements in C-EnKF-IRI during September 2017, which is derived during the forecasting phase. The computation of these measures follows the strategy presented in Fig. (4a).

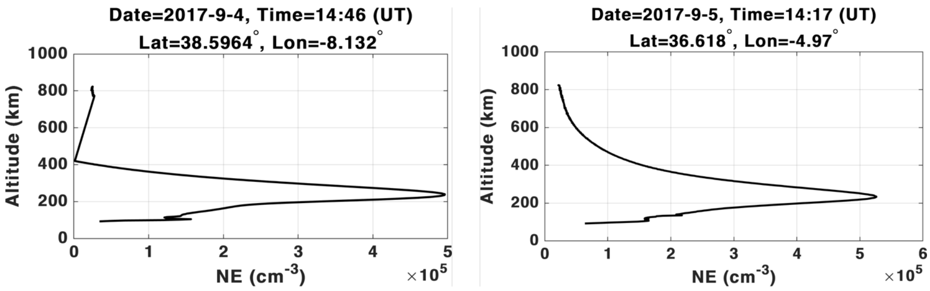

Fig. 8: Left: the failed electron density profile; Right: the accepted electron density profile observed by FORMOSAT-3/COSMIC based on the quality control tests (*Lei et al.*, 2007) and (*Yang et al.*, 2009).

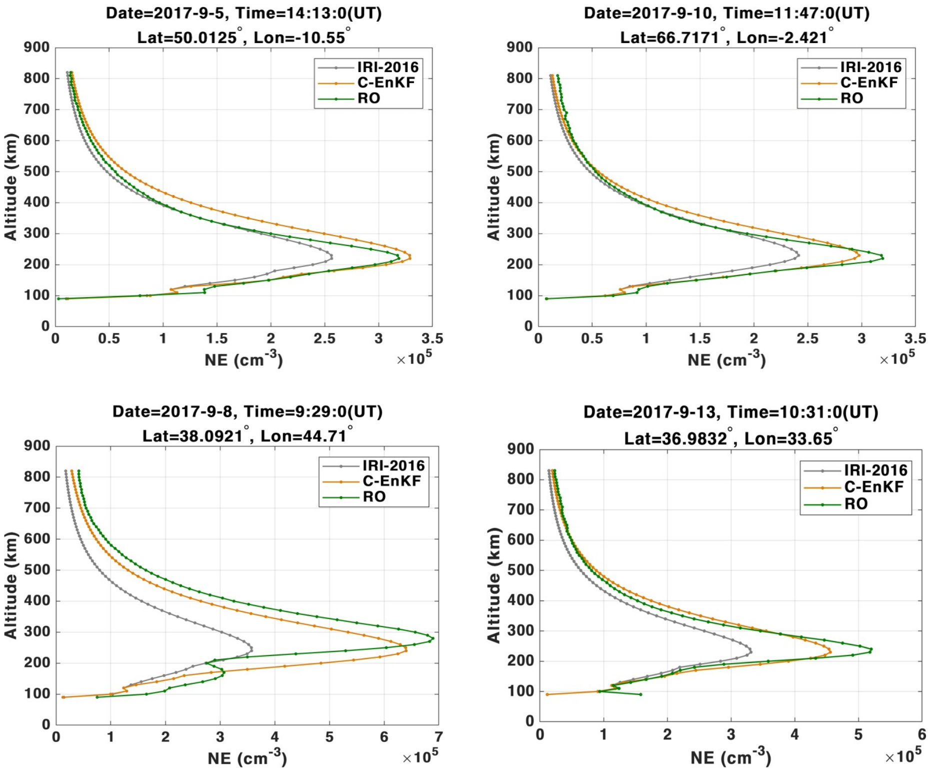

Fig. 9: The altitude-dependent profiles of Ne retrieved from the COSMIC radio occultation data, as well as the original IRI-2016, and C-EnKF-IRI. The COSMIC data are available within the European sector. Figures 9 (a-b) and (c-d) are related to the days with quite and storm conditions, respectively.

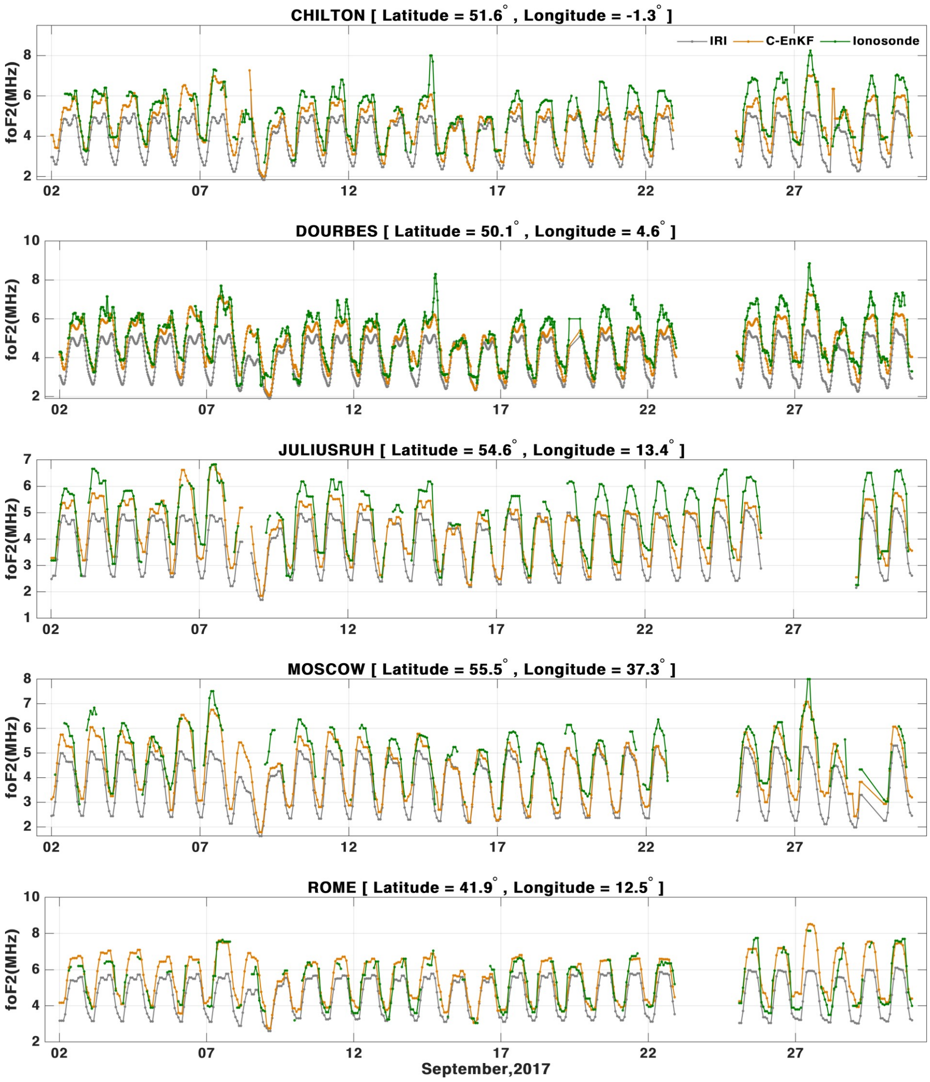

Fig. 10: Comparisons between $foF2$ values as measured by five ionosondes and the forecast of the original IRI-2016, as well as C-EnKF-IRI during September 2017.

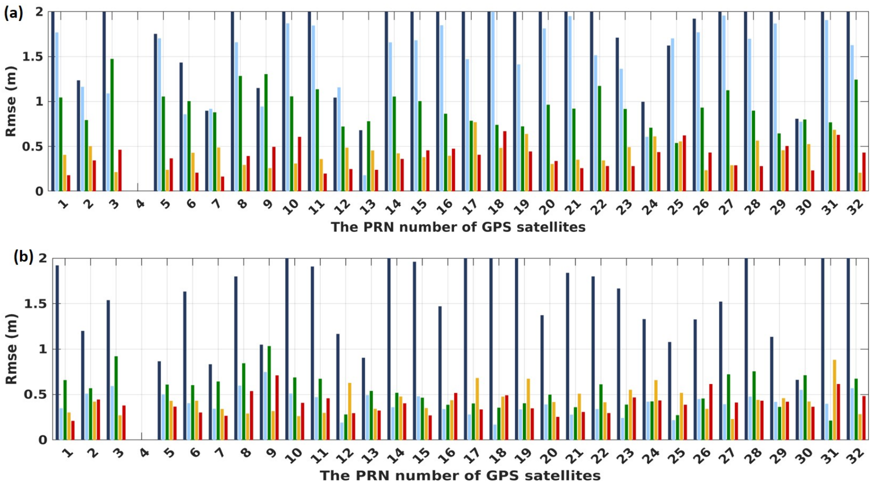

(a) GRAZ station (in Austria)

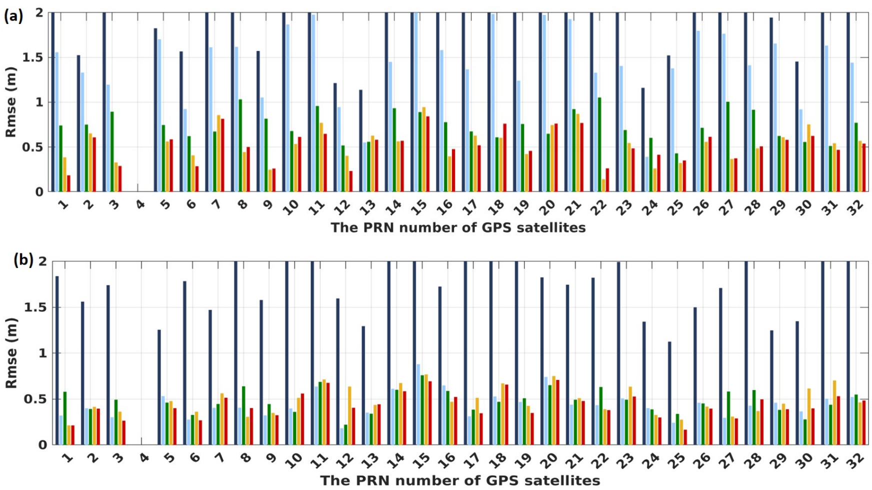

(b) PTBB station (in Germany)

Fig. 11: Differences between empirical slant ionospheric effects (from IRI-2016, C-EnKF-IRI, Klobuchar, NeQuick, as well as final product of IONEX fields) and those derived from processing dual frequency GPS measurements. Comparisons are performed on September 4^{st}, 2017 ('a') with high solar activity $F_{10.7} = 183$ sfu and on September 21^{th}, 2017 ('b') with low solar activity of $F_{10.7} = 73$ sfu.

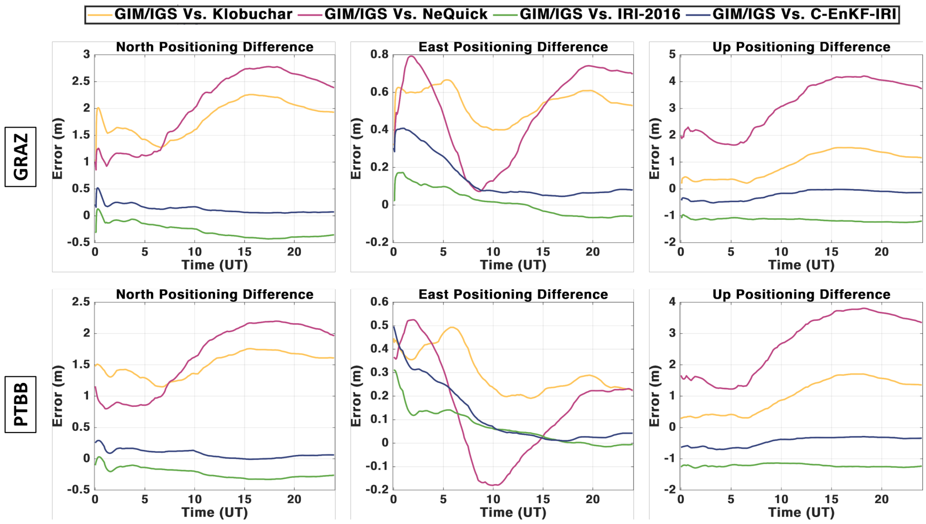

Fig. 12: Comparisons between computed position difference in the east, north and height direction for GRAZ (longitude: 15.493°E and latitude: 47.067°N in Austria) and PTBB (longitude: 10.460°E and latitude: 52.296°N in Germany) stations on 4 September 2017. The differences are measured with assumed that SPP solutions using IONEX product is reference.